

# Global models of planetary system formation in radiatively-inefficient protoplanetary discs

Phil Hellary<sup>1\*</sup> and Richard P. Nelson<sup>1</sup>

<sup>1</sup>*Astronomy Unit, Queen Mary University of London, Mile End Road, London, UK E1 4NS*

Accepted XXX. Received XXX.

## ABSTRACT

We present the results of N-body simulations of planetary systems formation in radiatively-inefficient disc models, where positive corotation torques may counter the rapid inward migration of low mass planets driven by Lindblad torques. The aim of this work is to examine the nature of planetary systems that arise from oligarchic growth in such discs. We adapt the commonly-used Mercury-6 symplectic integrator by including simple prescriptions for planetary migration (types I and II), planetary atmospheres that enhance the probability of planetesimal accretion by protoplanets, gas accretion onto forming planetary cores, and gas disc dispersal. We perform a suite of simulations for a variety of disc models with power-law surface density and temperature profiles, with a focus on models in which unsaturated corotation torques can drive outward migration of protoplanets. In some models we account for the quenching of corotation torques that arises when planetary orbits become eccentric. Approximately half of our simulations lead to the successful formation of gas giant planets with a broad range of masses and semimajor axes. Giant planet masses range from being approximately equal to that of Saturn, up to approximately twice that of Jupiter. The semimajor axes of these range from being  $\sim 0.2$  AU, up to  $\sim 75$  AU, with disc models that drive stronger outward migration favouring the formation of longer-period giant planets. Out of a total of 20 giant planets being formed in our simulation suite, we obtain 3 systems that contain two giants. No super-Earth or Neptune-mass planets were present in the final stages of our simulations, in contrast to the large abundance of such objects being discovered in observation surveys. This result arises because of rapid inward migration suffered by massive planetary cores that form early in the disc life time (for which the corotation torques saturate), combined with gas accretion onto massive cores that leads them to become gas giants. Numerous low mass planets are formed and survive in the simulations, with masses ranging from a few tenths of an Earth mass, up to  $\sim 3$  Earth masses. Simulations in which the quenching of corotation torques for planets on modestly eccentric orbits was included failed to produce any giant planets, apparently because Lindblad torques induce rapid inward migration of planetary cores in these systems.

We conclude that convergent migration induced by corotation torques operating during planet formation can enhance the growth rate of planetary cores, but these often migrate into the central star because corotation torques saturate. Outward migration of planetary cores of modest mass can lead to the formation of gas giant planets at large distances from the central star, similar to those observed recently through direct imaging surveys. The excitation of planetary eccentricities through planet-planet scattering during oligarchic growth may quench the effects of corotation torques, however, such that inward migration is driven by Lindblad torques.

**Key words:** planetary systems, planets and satellites: formation, planet-disc interactions, protoplanetary discs

## 1 INTRODUCTION

Observations of extrasolar planets are providing a picture of a highly diverse population of bodies orbiting

\* E-mail: p.hellary@qmul.ac.uk

main sequence stars. At the extreme ends of the distribution, there exist very short-period low-mass rocky planets such as CoRoT-7b (Léger et al. 2009) and Kepler-10b (Batalha et al. 2011), and very long-period massive gas giant planets detected in recent years by direct imaging (Marois et al. 2010; Kalas et al. 2008; Lagrange et al. 2010). In addition, there have been discoveries of short-period hot-Jupiters such as 51-Pegb (Mayor & Queloz 1995), hot-Neptunes such as Gliese 436b (Butler et al. 2004), and super-Earths such as Gliese 581c (Bonfils et al. 2005). Multiple planet systems are common, examples being the five planet system orbiting the star 55 Cancri consisting of gas giants and Neptune-mass bodies (Fischer et al. 2008), and the recently reported Kepler-11 system, consisting of six nearly coplanar low-mass planets (Lissauer et al. 2011). A question that needs to be addressed is whether or not a particular model of planet formation, such as the core-accretion model, can explain this broad diversity, appealing to variety in the planet forming environment to explain the range of observed systems. Or is it the case that quite different physical processes are operating on different length and/or time scales within protoplanetary discs to form planets with very different characteristics. For example, core-accretion operating on long-timescales at relatively close locations to the central star to form short-period systems, and disc gravitational fragmentation occurring at large radii on short-timescales to form long-period giant planets.

To begin addressing this question in detail, it is necessary to construct global models of planetary formation that allow for the formation of multiple planet systems with a diversity of masses and orbital elements (semimajor axes, eccentricities etc). In this paper, we present the results from global models, that are based on the oligarchic growth scenario for planet formation, that have been constructed using a symplectic N-body code (Chambers 1999), in conjunction with simplified prescriptions for the gas disc model, planetary migration, capture of planetesimals, gas-envelope accretion, and disc dispersal on Myr time scales. One of our main objectives in this work is to examine how our current understanding of migration of low-mass planets influences the formation of planetary systems, with particular emphasis on the corotation torques in radiatively-inefficient discs (Paardekooper et al. 2010; Paardekooper, Baruteau, & Kley 2011). As we anticipate that this is the first paper in a series that will examine this issue, the prescriptions we have adopted in this initial study for a number of physical processes, such as gas accretion, are necessarily very simplified. They serve the useful purpose, however, of enabling N-body simulations to be performed of planetary system formation that lead to a diversity of outcomes, and these can be used to guide future model developments.

There is a substantial body of previous work that has examined the role of migration in the formation of planets using N-body simulations. Papaloizou & Larwood (2000) examined planetary growth through planet-planet collisions using N-body simulations combined with prescriptions for migration and eccentricity/inclination damping. McNeil, Duncan, & Levison (2005) and Daisaka et al. (2006) examined the effect of type I migration on terrestrial planet formation, and Fogg & Nelson (2007, 2009) examined the influence of type I migration on the

formation of terrestrial planets in the presence of migrating Jovian-mass planets. Terquem & Papaloizou (2007) examined the formation of hot-super-Earths and hot-Neptunes using N-body simulations with type I migration. McNeil & Nelson (2009, 2010) carried out large-scale simulations of oligarchic growth to explore the formation of systems of hot-Neptunes and super-Earths, such those around the stars Gliese 581 and HD698433, using a novel symplectic integrator with multiple timesteps. An alternative to these approaches has been planetary population synthesis modelling, as presented by Ida & Lin (2008, 2010), Mordasini, Alibert, & Benz (2009a), Mordasini et al. (2009b), and Miguel, Guilera, & Brunini (2011). These monte-carlo approaches have significant advantages in being able to cover a very broad range of parameter space, allowing meaningful statistical comparisons with observational data to be undertaken. The computational efficiency also allows complex models of planetary atmospheres and gas accretion to be incorporated, as presented by the Mordasini et al work. Accurate treatment of planet-planet gravitational interactions are difficult to include in these models, however, such that predictions about planetary system multiplicity, orbital eccentricities and inclinations are not a natural outcome of the models (we note that models by Ida & Lin (2010) now include a simplified treatment of planet-planet interaction dynamics).

This paper is organised as follows. In Sect. 2 we present the numerical methods and the physical model. In Sect. 3 we present the initial conditions for the simulations. Results are described and analysed in Sect. 4, comparisons are made to observations in Sect. 5 and a discussion and concluding remarks are provided in Sect. 6.

## 2 METHOD

In the following subsections we give details about our physical model and the numerical methods we employ.

### 2.1 Gas disc model

To limit the parameter space covered by the simulations, we consider only disc models that can provide outward migration when unsaturated corotation torques are included. The conditions under which outward migration occurs are discussed in later sections, but as a rule of thumb we find that the temperature radial power-law index,  $\beta$ , must be approximately 0.25 larger than the surface density power-law index,  $\alpha$ .

The gas surface density is given by the power-law expression

$$\Sigma_g(R, t) = \Sigma_g(1 \text{ AU}) \left( \frac{R}{1 \text{ AU}} \right)^{-\alpha} \exp(-t/\tau_{\text{disc}}) \quad (1)$$

where the factor  $\exp(-t/\tau_{\text{disc}})$  mimics the dispersal of the gas disc by viscous evolution and photoevaporation on a time scale defined by  $\tau_{\text{disc}}$ . The volume density of gas is then

$$\rho(R, z, t) = \frac{\Sigma(R, t)}{\sqrt{2\pi}H} \exp(-z^2/2H^2) \quad (2)$$

where  $H$  is the local disc scale height. The disc temperature is also given by a power-law function of radius

$$T(R) = T(1 \text{ AU}) \left( \frac{R}{1 \text{ AU}} \right)^{-\beta}. \quad (3)$$

A disc with power-law density and temperature profiles also has a power-law entropy profile. The associated power-law index is given by

$$\zeta = (\alpha + \beta) - \alpha\gamma \quad (4)$$

where  $\gamma$  is the usual ratio of specific heats, here taken to be  $\gamma = 7/5$ . The isothermal sound speed is

$$c_s = \sqrt{\frac{k_B T}{m_H \mu}} \quad (5)$$

where  $k_B$  is the Boltzmann constant,  $m_H$  is the mass of a hydrogen atom and  $\mu$  is the mean molecular weight (here assumed to equal 2.4). The disc scale height is given by

$$H = c_s \Omega_K \quad (6)$$

where  $\Omega_K$  is the Keplerian angular velocity. The angular velocity of the gas is given by

$$\Omega(R) = \Omega_K(R) \left[ 1 - (\alpha + \beta) \left( \frac{H}{R} \right)^2 \right]. \quad (7)$$

## 2.2 Opacities

We take the opacity  $\kappa$  to be always equal to the Rosseland mean opacity, and we take the temperature and density dependence to be given by the formulae of Bell et al. (1997) below 3730 K and by Bell & Lin (1994) above this value:

$$\kappa[\text{cm}^2/\text{g}] = \begin{cases} 10^{-4} T^{2.1} & T < 132 \text{ K} \\ 3 T^{-0.01} & 132 \text{ K} \leq T < 170 \text{ K} \\ T^{-1.1} & 170 \text{ K} \leq T < 375 \text{ K} \\ 5 \times 10^4 T^{-1.5} & 375 \text{ K} \leq T < 390 \text{ K} \\ 0.1 T^{0.7} & 390 \text{ K} \leq T < 580 \text{ K} \\ 2 \times 10^{15} T^{-5.2} & 580 \text{ K} \leq T < 680 \text{ K} \\ 0.02 T^{0.8} & 680 \text{ K} \leq T < 960 \text{ K} \\ 2 \times 10^{81} \rho T^{-24} & 960 \text{ K} \leq T < 1570 \text{ K} \\ 10^{-8} \rho^{2/3} T^3 & 1570 \text{ K} \leq T < 3730 \text{ K} \\ 10^{-36} \rho^{1/3} T^{10} & 3730 \text{ K} \leq T < 10000 \text{ K} \end{cases} \quad (8)$$

## 2.3 Disc solid component

The disc solid component is composed initially of protoplanets and planetesimals (that we model as a computationally feasible number of ‘superplanetesimals’ of much larger mass than real planetesimals, but with an assumed radius equal to that of realistic planetesimals (10 km) such that they experience the appropriate gas drag force.) Protoplanets are initially spaced by 10 mutual Hill radii, and planetesimals are scattered throughout the disc such that the total solids content follows the surface density power-law prescribed for the

gaseous component. As in Thommes et al. (2003), planetesimals are distributed according to a Rayleigh distribution and have RMS values of the eccentricity  $e = 0.01$  and inclination  $i = 0.005$  radians, respectively. The surface density of solids is enhanced beyond the snow line, whose position  $R_{\text{snow}}$  is determined by the location where the temperature falls below 170 K. The snow line discontinuity is spread over a distance  $\sim 1$  AU:

$$\Sigma_{s,0}(R) = \left\{ \Sigma_1 + (\Sigma_2 - \Sigma_1) \left[ \frac{1}{2} \left( \frac{R - R_{\text{snow}}}{0.5 \text{ AU}} \right) + \frac{1}{2} \right] \right\} \left( \frac{R}{1 \text{ AU}} \right)^{-\alpha} \quad (9)$$

The surface density enhancement due to the snowline ( $\Sigma_2/\Sigma_1 = 30/7.1$  as in Thommes et al. (2003)). Planetesimal densities are set at  $3 \text{ g/cm}^3$  throughout the disk. Protoplanet densities are set at  $3 \text{ g/cm}^3$  inside the snowline and  $1.5 \text{ g/cm}^3$  beyond, as defined by Thommes et al. (2003). The mass of the protoplanets at  $t = 0$  is  $m_p = 0.02 M_{\oplus}$ , and the mass of the superplanetesimals is  $0.004 M_{\oplus}$ .

## 2.4 Aerodynamic drag

For kilometre-sized planetesimals, aerodynamic drag provides an efficient source of eccentricity and inclination damping. We apply gas drag to all bodies in the simulation in the form of Stokes’ drag law (Adachi et al. 1976),

$$\mathbf{F}_{\text{drag}} = m_p \left( \frac{-3\rho C_D}{8\rho_p r_p} \right) v_{\text{rel}} \mathbf{v}_{\text{rel}} \quad (10)$$

where  $\rho$  is the local gas density,  $\rho_p$  is the density of the planetesimal,  $r_p$  is the radius of the body and  $C_D$  is a dimensionless drag coefficient (here taken to be unity).

## 2.5 Capture radii enhancement due to atmospheric drag

If a protoplanet becomes large enough to accumulate a gaseous atmosphere, the gas drag acting on planetesimals passing through this atmosphere has the effect of increasing the effective capture radius. We use the prescription described in section 2.5 of Inaba & Ikoma (2003) to model this effect (see their Eq. 17 and appendix A). In this model, a planetesimal that is within the Hill sphere of the protoplanet, and located a distance  $r_c$  from the centre of the protoplanet, will be captured if its physical radius is less than  $r_{\text{crit}}$  given by the expression

$$r_{\text{crit}} = \frac{3 v_{\text{rel}}^2 + 2Gm_p/r_c}{2 v_{\text{rel}}^2 + 2Gm_p/r_H} \frac{\rho(r_c)}{\rho_p}. \quad (11)$$

Here  $\rho(r_c)$  is the local density of the protoplanet atmosphere,  $\rho_p$  is the density of the planetesimal,  $r_H$  is the protoplanet’s Hill radius and  $v_{\text{rel}}$  is the relative velocity between the two bodies.

The atmosphere model requires us to specify the luminosity of the planet. We assume that this is equal to the gravitational energy released by incoming planetesimals

$$L_p = \frac{Gm_p}{r_p} \frac{dm_p}{dt} \quad (12)$$

We monitor the accretion rate of solids experienced by protoplanets in our simulations, and use this to determine the accretion luminosity. In order to smooth out the stochastic nature of planetesimal accretion, we calculate and use the

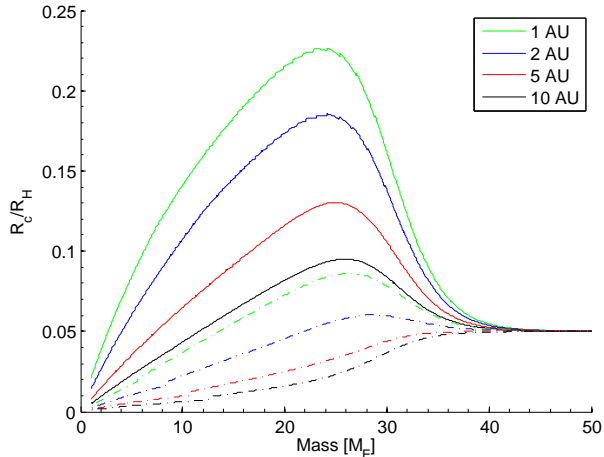


**Figure 1.** Effective planetesimal capture radius enhancement due to atmospheric drag for 10 km planetesimals and with various planet luminosities. Solid lines correspond to  $L_p = 10^{-8} L_\odot$ ; dot-dashed lines correspond to  $L_p = 10^{-5} L_\odot$ .

average luminosity of a protoplanet over temporal windows of 200 local orbits (or 4000 years, whichever is smaller). We limit the calculated luminosity to within the range  $10^{-9}$  to  $10^{-4} L_\odot$ .

The Inaba & Ikoma (2003) model assumes that the contribution to the gravitating mass from the atmosphere is negligible compared to that of the solid core. In order to avoid an overestimation of the capture radius of larger planets, we limit the effective capture radius of a planet to be a maximum of 1/20 of a planet’s Hill radius for these planets. The transition is smoothed using the expression

$$r_{\text{capture}} = \left[ 0.5 - 0.5 \tanh \left( \frac{m_p - 30M_\oplus}{5M_\oplus} \right) \right] r_{\text{atmos}} + \left[ 0.5 + 0.5 \tanh \left( \frac{m_p - 30M_\oplus}{5M_\oplus} \right) \right] 0.05r_H \quad (13)$$

where  $r_{\text{capture}}$  is the effective capture radius,  $r_{\text{atmos}}$  is the enhanced capture radius due to the atmosphere and  $r_H$  is the Hill radius. Figure 1 shows the effective capture radius as a function of planet mass and luminosity, including the above smoothing procedure.

## 2.6 Type I migration in radiatively-inefficient discs

We include the migration of low mass planets in our simulations by implementing the torque formulae presented by Paardekooper et al. (2010) and Paardekooper, Baruteau, & Kley (2011). These formulae describe how the various torque contributions vary as the planet mass and local conditions in the disc change. Specifically, corotation torques depend sensitively on the ratio of the horseshoe libration time scale to either the viscous or thermal diffusion time scales.

There are two basic contributions to the corotation torque: the vorticity-related corotation torque and the entropy-related corotation torque. In an inviscid two dimensional disc, the vortensity (ratio of vorticity to surface density) is a conserved quantity on streamlines. Fluid elements undergoing horseshoe orbits in the presence of a

planet therefore conserve this quantity. For power-law surface density profiles with indices greater (less negative) than  $-3/2$ , there is a negative radial vortensity gradient, and the exchange of angular momentum between an embedded planet and disc material as the fluid follows horseshoe streamlines generating a positive torque on the planet (Goldreich & Tremaine 1979). In the absence of viscous diffusion, material undergoing horseshoe orbits eventually phase mixes because of the varying horseshoe orbit time scales, erasing the vortensity profile in the corotation region and saturating the corotation torque (i.e. switching it off). The action of viscous stresses can desaturate the horseshoe torque by maintaining the vortensity gradient across the horseshoe region, and this occurs optimally when the viscous diffusion time scale across the width of the horseshoe region is approximately equal to half the horseshoe libration time. The presence of horseshoe streamlines inevitably means that the associated horseshoe torque is a non linear effect (because horseshoe orbits are not present in a linear theory), usually referred to as horseshoe drag (Ward 1991; Masset 2001; Paardekooper & Papaloizou 2008). As the viscosity is increased above its optimal value the vortensity on streamlines begins to be modified significantly as the fluid undergoes horseshoe U-turns. For large enough viscosity the vorticity-related corotation torque eventually approaches the smaller value obtained from linear theory (Masset 2002). This arises when the viscous diffusion time is shorter than the horseshoe U-turn time.

A similar process occurs for the entropy-related corotation torque, but in this case the controlling parameter is the thermal diffusion time scale instead of the viscous one. Optimal corotation torques are obtained when both the thermal and viscous diffusion time scales across the width of the horseshoe region are equal to approximately half the horseshoe libration time. It should be noted that, in addition to thermal diffusion, viscosity is required to desaturate the entropy-related horseshoe torque. This is because material trapped in the horseshoe region in an inviscid disc constitutes a closed system that can only exchange a finite quantity of angular momentum with the planet. Viscosity is required to couple this region with the rest of the disc, such that exchange of angular momentum can desaturate the corotation torque.

For simplicity of implementation we adopt the approximation suggested by Lyra, Paardekooper, & Mac Low (2010) and assume that the thermal and viscous time scales in the disc are equal. For a disc in thermodynamic equilibrium, where the heating is provided by viscous dissipation and local cooling is via blackbody radiation, this is a reasonable assumption to make.

Based on the above discussion, the torque experienced by a low mass planet embedded in a disc depends on the Lindblad torques (originating from the excitation of density waves at Lindblad resonances), and a weighted sum of the vorticity-related horseshoe drag, the entropy-related horseshoe drag, the vorticity-related linear corotation torque, and the entropy-related linear corotation torque. These torque contributions are given as follows:

The Lindblad torque is

$$\Gamma_{\text{LR}} = \left( \frac{\Gamma_0}{\gamma} \right) [-2.5 - 1.7\beta + 0.1\alpha] \quad (14)$$

the vorticity-related horseshoe drag is

$$\Gamma_{\text{VHS}} = \left(\frac{\Gamma_0}{\gamma}\right) \left[1.1 \left(\frac{3}{2} - \alpha\right)\right] \quad (15)$$

the entropy-related horseshoe drag is

$$\Gamma_{\text{EHS}} = \left(\frac{\Gamma_0}{\gamma}\right) \left[7.9 \frac{\zeta}{\gamma}\right] \quad (16)$$

the vorticity-related linear corotation torque is

$$\Gamma_{\text{LVCT}} = \left(\frac{\Gamma_0}{\gamma}\right) \left[0.7 \left(\frac{3}{2} - \alpha\right)\right] \quad (17)$$

the entropy-related linear corotation torque is

$$\Gamma_{\text{LECT}} = \left(\frac{\Gamma_0}{\gamma}\right) \left[\left(2.2 - \frac{1.4}{\gamma}\right) \zeta\right] \quad (18)$$

In these above expression  $\gamma$  is the ratio of specific heats, and  $\Gamma_0$  is given by

$$\Gamma_0 = \left(\frac{m_p}{M_*}\right) \left(\frac{m_p}{\Sigma_p a_p^2}\right) \left(\frac{a_p \Omega_p}{c_s}\right)^2 a_p^2 \Omega_p^2, \quad (19)$$

where  $a_p$  is the planet semimajor axis, and a subscript ‘p’ denotes that quantities should be evaluated at the orbital location of the planet. In order to obtain the correct total torque as a function of the thermal and viscous diffusion coefficients we combined the above individual torque expressions into the following formula (Paardekooper, Baruteau, & Kley 2011):

$$\Gamma_{\text{tot}} = \Gamma_{\text{LR}} + \left\{ \Gamma_{\text{VHS}} F_\nu G_\nu + \Gamma_{\text{EHS}} F_d F_d \sqrt{G_\nu G_d} \right. \\ \left. + \Gamma_{\text{LVCT}} (1 - K_\nu) + \Gamma_{\text{LECT}} (1 - K_\nu) (1 - K_d) \right\} E \quad (20)$$

where the functions  $G_\nu$ ,  $G_d$ ,  $F_\nu$ ,  $F_d$ ,  $K_\nu$  and  $K_d$  are related either to the ratio between the viscous/thermal diffusion time scales and the horseshoe libration time scale, or to the ratio of the viscous/thermal diffusion time scales and the horseshoe U-turn time scale. The factor  $E$ , that multiplies all terms that can contribute to the corotation torque, allows for the fact that corotation torques may be strongly attenuated when the planet has a finite eccentricity, such that it undergoes radial excursions that are larger than the width of the horseshoe region (Bitsch & Kley 2010). To account for this effect we define  $E$  according to

$$E = (1 - \tanh(e/x_s)). \quad (21)$$

where the dimensionless horseshoe width is given by

$$x_s = \frac{1.1}{\gamma^{1/4}} \sqrt{\frac{q}{h}}, \quad (22)$$

$q = m_p/M_*$  and  $h = H/R$ . Note that for most simulations we set  $E = 1$ , but for a subsample of our runs (labelled as ‘E’) we use Eq. (21) to define  $E$ .

The horseshoe libration time is given by  $t_{\text{lib}} = 8\pi/(3\Omega_p x_s)$ , and the viscous diffusion time scale across the horseshoe region is given by  $t_\nu = (x_s a_p)^2/\nu$ , where  $\nu$  is the viscous diffusion coefficient. Similarly the thermal diffusion time scale is given by  $t_d = (x_s a_p)^2/D$ , where  $D$  is the thermal diffusion coefficient (defined below). Following Paardekooper, Baruteau, & Kley (2011), we define two parameters that determine the relation between the thermal/diffusion time scales and the horseshoe libration time

scale

$$p_\nu = \frac{2}{3} \sqrt{\frac{a_p^2 \Omega_p x_s^3}{2\pi\nu}} \equiv \sqrt{\frac{16}{27} \frac{t_\nu}{t_{\text{lib}}}}, \quad (23)$$

which we refer to as the viscous diffusion parameter

$$p_d = \sqrt{\frac{a_p^2 \Omega_p x_s^3}{2\pi D}} \equiv \sqrt{\frac{4}{3} \frac{t_d}{t_{\text{lib}}}}, \quad (24)$$

which we refer to as the thermal diffusion parameter. Note that  $\nu$  and  $D$  are assumed to be equal in this work, and are complicated functions of radial position in the disc because of the functional form used to define the opacity in Eq. (8). These diffusion parameters are used to define the following functions

$$F_\nu = \frac{1}{[1 + (p_\nu/1.3)^2]} \quad (25)$$

$$F_d = \frac{1}{[1 + (p_d/1.3)^2]}. \quad (26)$$

Using the viscous diffusion parameter  $p_\nu$  we also define the following functions

$$G_\nu = \begin{cases} \frac{16}{25} \left(\frac{45\pi}{8}\right)^{3/4} p_\nu^{3/2} & \text{if } p_\nu < \sqrt{8/(45\pi)} \\ 1 - \frac{9}{25} \left(\frac{8}{45\pi}\right)^{4/3} p_\nu^{-8/3} & \text{if } p_\nu \geq \sqrt{8/(45\pi)} \end{cases} \quad (27)$$

$$K_\nu = \begin{cases} \frac{16}{25} \left(\frac{45\pi}{28}\right)^{3/4} p_\nu^{3/2} & \text{if } p_\nu < \sqrt{8/(45\pi)} \\ 1 - \frac{9}{25} \left(\frac{28}{45\pi}\right)^{4/3} p_\nu^{-8/3} & \text{if } p_\nu \geq \sqrt{28/(45\pi)} \end{cases} \quad (28)$$

Using the thermal diffusion parameter  $p_d$  we define the following functions

$$G_d = \begin{cases} \frac{16}{25} \left(\frac{45\pi}{8}\right)^{3/4} p_d^{3/2} & \text{if } p_d < \sqrt{8/(45\pi)} \\ 1 - \frac{9}{25} \left(\frac{8}{45\pi}\right)^{4/3} p_d^{-8/3} & \text{if } p_d \geq \sqrt{8/(45\pi)} \end{cases} \quad (29)$$

$$K_d = \begin{cases} \frac{16}{25} \left(\frac{45\pi}{28}\right)^{3/4} p_d^{3/2} & \text{if } p_d < \sqrt{28/(45\pi)} \\ 1 - \frac{9}{25} \left(\frac{28}{45\pi}\right)^{4/3} p_d^{-8/3} & \text{if } p_d \geq \sqrt{28/(45\pi)} \end{cases} \quad (30)$$

### 2.6.1 Thermal and viscous diffusion

Radiative diffusion in the disc causes the thermal energy per unit volume,  $e$ , to evolve according to

$$\frac{\partial e}{\partial t} = -\nabla \cdot \mathbf{F} \quad (31)$$

where the radiative flux in the radial direction (across the horseshoe region) may be expressed as

$$F_r = -\frac{4a_r c T^3}{3 \kappa_r \rho} \frac{dT}{dr}. \quad (32)$$

Here  $a_r$  is the radiation constant and  $c$  is the speed of light. Noting that  $e = P/(\gamma - 1)$  and  $P = k_B \rho T/(\mu m_H)$ , and assuming that  $\rho$  is locally constant, we obtain the diffusion equation governing temperature evolution

$$\frac{\partial T}{\partial t} = \nabla_r \left( D \frac{dT}{dr} \right) \quad (33)$$

where the diffusion coefficient,  $D$ , is given by

$$D = \frac{4a_r c T^3 (\gamma - 1) \mu m_H}{3 \kappa \rho^2 k_B}. \quad (34)$$

We set the viscous diffusion coefficient equal to the thermal diffusion coefficient for the purpose of determining the level of saturation of corotation torques ( $\nu = D$ ).

### 2.6.2 Eccentricity and inclination damping

To damp the inclinations of protoplanets we used the prescription given in Appendix A of Daisaka et. al. (2006):

$$F_{idamp,z} = m_p \left( \frac{m_p}{M_\odot} \right) \left( \frac{a_p \Omega_p}{c_s} \right)^4 \left( \frac{\Sigma_g a_p^2}{M_\odot} \right) \Omega_p (2A_z^c v_z + A_z^s z \Omega_p) \quad (35)$$

where  $A_z^c = -1.088$  and  $A_z^s = -0.871$ .

To damp eccentricities we used a simple time scale damping formula given by

$$F_{edamp,r} = -\frac{v_r}{t_{edamp}}, \quad F_{edamp,\theta} = -\frac{0.5(v_\theta - v_K)}{t_{edamp}} \quad (36)$$

where

$$t_{edamp} = \left( \frac{m_p}{M_\odot} \right)^{-1} \left( \frac{a_p \Omega_p}{c_s} \right)^{-4} \left( \frac{\Sigma_g a_p^2}{M_\odot} \right)^{-1} \Omega_p^{-1} \quad (37)$$

This prescription was adopted rather than using the eccentricity damping forces prescribed in Daisaka et. al. (2006) because we found that they could generate significant jitter in the acceleration experienced by the planets in disc models with strong radial temperature gradients, where  $H/r$  becomes small near the disc outer edge. The formula based on the time scale argument produced smoother results, apparently because it is based on an orbit-averaging procedure rather than capturing the instantaneous force experienced by a planet around its orbit.

## 2.7 Gas envelope accretion

As protoplanets grow through mutual collision and planetesimal accretion they are able to accrete a gaseous envelope from the surrounding disc, and may eventually become gas giant planets. To model gaseous envelope accretion, we have implemented a very approximate scheme by calculating fits to the results of 1D giant planet formation calculations presented by Movshovitz et al. (2011). Working in time units of Myr and mass units of Earth masses, the gas accretion rate is given by

$$\frac{dm_{ge}}{dt} = 5.5 \left( \frac{1}{\tau_{ge} - \tau_{ge0}} \right) \quad (38)$$

where we define  $\tau_{ge}$  by the expression

$$\tau_{ge} = 9.665 M_{\text{core}}^{-1.2}, \quad (39)$$

and  $\tau_{ge0}$  is given by the expression

$$\tau_{ge0} = \tau_{ge} \left( 1 - \left( \frac{1}{\exp\left(\frac{m_{ge}}{5.5}\right)} \right) \right). \quad (40)$$

This procedure allows the planet core to grow due to accretion of solids after envelope accretion has commenced, and allows the rate of envelope accretion to adjust to the changing core mass. It is well known from the studies of

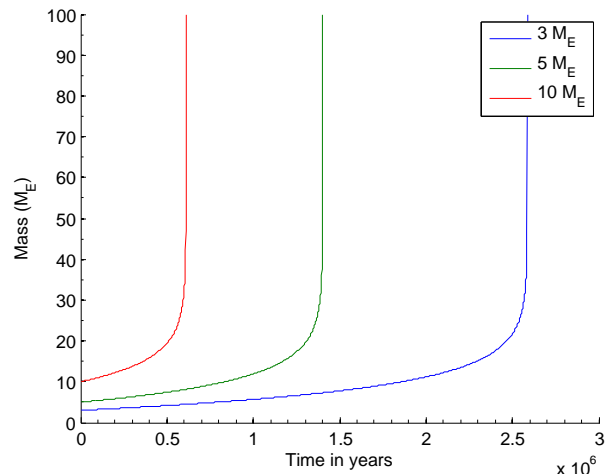


**Figure 2.** Gas accretion onto giant planet cores for 3, 5 and 10  $M_\oplus$  cores against time at 5 AU in a disc with no migration or planetesimal accretion.

Pollack et al. (1996) and others that the rate of gas envelope accretion is a sensitive function of the core mass, increasing as the core mass increases. Figure 2 shows the gas envelope mass evolution in the absence of planetesimal accretion and migration for planets with fixed core mass. These are very similar to the results of detailed 1D giant planet formation calculations displayed in figure 1 of Movshovitz et al. (2011). Although we have implemented the above equations for gas accretion numerically, we note that they have the analytic solution

$$m_{ge}(t) = -5.5 \ln \left( 1 - \frac{m_{\text{core}}^{1.2}}{9.665} t \right). \quad (41)$$

Ideally, we would like to incorporate full 1D models of giant planet formation in our N-body simulations, such that the gas envelope accretion can respond to the changing planetesimal accretion rate and changing conditions in the disc, but such an approach is computationally prohibitive at present. Our simplified approach is highly efficient and provides a reasonably good approximation to detailed core nucleated accretion models, enabling us to add a vital missing component to our N-body simulations.

The amount of gas that can accrete rapidly onto a forming giant planet is constrained by the availability of gas in the local feeding zone. We allow giant planets to accrete gas using the procedure described above until the envelope mass approaches the isolation mass, defined to be the gas mass in the feeding zone. We approximate the feeding zone width to be (Lissauer 1993)

$$r_c = 2\sqrt{3}r_H \quad (42)$$

leading to the following expression for the gas isolation mass of the planet

$$m_{g\text{-iso}} = \int_{a-2\sqrt{3}r_H}^{a+2\sqrt{3}r_H} 2\pi \Sigma_g R dR. \quad (43)$$

During the growth of the planet, it can begin to open a gap through nonlinear tidal interaction with the disc (Lin & Papaloizou 1986) and for typical disc parameters this

occurs around a Jovian mass (Bryden et al. 1999; Kley 1999; Nelson et al. 2000). Consequently, if the isolation mass exceeds the Jovian mass, we limit the mass of the planet that can be obtained during runaway gas accretion to be the Jovian mass.

Once the runaway cut-off mass has been reached, the gas accretion rate switches to the rate that viscosity can supply mass to the planet from the gas disc,

$$\frac{dm_{\text{ge}}}{dt} = 3\pi\nu\Sigma_{\text{g}} \quad (44)$$

where  $\nu$  is the local disc viscosity given by

$$\nu = \alpha_{\nu} H^2 \Omega(R) \quad (45)$$

where  $\alpha_{\nu}$  is the viscous parameter (set to  $10^{-3}$  for the purpose of this calculation). Note that this value for the kinematic viscosity is not the same as that obtained by assuming the thermal and viscous diffusion coefficients are equal, as is done to determine the magnitude of the corotation torques acting on a planet (see Sect. 2.6). However, the value of  $\alpha_{\nu}$  adopted for the purpose of determining the viscously-driven mass accretion rate is similar to that used in many previous studies of disc-planet interactions (Bryden et al. 1999; Kley 1999; Nelson et al. 2000), and produces viscous accretion rates within the range observed to occur onto T Tauri stars (Sicilia-Aguilar et al. 2004).

## 2.8 Type II migration

For massive planets, the migration changes from being of type I to being of type II as gap formation occurs. Under these circumstances the planet migrates inward on a time scale equal to the local viscous evolution time,  $\tau_{\nu}$ , provided that the planet mass is smaller than the local disc mass. For more massive planets the migration slows down due to the inertia of the planet (and is ultimately determined by the time over which the viscous flow in the disc delivers a mass of gas comparable to that of the planet to the planet orbital radius (Ivanov, Papaloizou, & Polnarev 1999; Syer & Clarke 1995)).

The viscous evolution time is  $\tau_{\nu} = R^2/(3\nu)$ , where we use Eqn. 45 to calculate  $\nu$ , and we apply the following torque in the type II migration regime

$$\Gamma_{\text{II}} = -\frac{m_{\text{p}} j_{\text{p}}}{\tau_{\nu}} \left(1 + \frac{m_{\text{p}}}{\pi a_{\text{p}}^2 \Sigma_{\text{p}}}\right)^{-1} \quad (46)$$

where  $m_{\text{p}}$  is the planet mass,  $j_{\text{p}}$  is the specific angular momentum,  $a_{\text{p}}$  is the planet semimajor axis and  $\Sigma_{\text{p}}$  is the disc surface density at the planet's semimajor axis location. We transition smoothly between the type I and type II migration regimes using the following expression

$$\Gamma_{\text{eff}} = \Gamma_{\text{II}} B + \Gamma_{\text{I}}(1 - B) \quad (47)$$

where  $\Gamma_{\text{eff}}$  is the torque applied during the transition,  $\Gamma_{\text{I}}$  is the type I torque, and the transition function  $B$  is given by

$$B = 0.5 + 0.5 \tanh\left(\frac{m_{\text{p}} - 65M_{\oplus}}{15M_{\oplus}}\right). \quad (48)$$

This form for  $B$  was adopted to allow the transition to type II migration to begin for  $m_{\text{p}} = 30M_{\oplus}$ , and for the transition to be complete for planets with mass  $m_{\text{p}} = 100M_{\oplus}$ , in broad agreement with the results from analytic considerations

(Ward 1997) and numerical simulations (D'Angelo et al. 2003). In the type II regime, eccentricities and inclinations are damped on a time scale equal to  $\tau_{\nu}/10$ .

## 3 INITIAL CONDITIONS

Our simulations were performed using the Mercury-6 symplectic integrator (Chambers 1999), modified to include the physics described in Sect. 2. In order to model feasibly multiple parameter sets over time scales of 3 Myr, our planetesimal disc consists of super-planetesimals ( $0.004 M_{\oplus}$ ) with effective radius of 10km, representing the averaged orbits of a much larger number of real planetesimals. We set the mass of our protoplanets to be a factor of 5 larger than the planetesimals, giving run times of approximately three cpu weeks for each simulation.

To enable broad coverage of the  $\alpha$  and  $\beta$  parameter set, we limited the number of realisations of initial conditions to two runs for each parameter choice, with each member of the pair differing only by the random number seed used to determine initial positions of the planetesimals. Our initial suite of simulations included models with enhancements by factors of 3 and 5 above the mass of the Minimum Mass Solar Nebula (MMSN) (Hayashi 1981) (models labelled 'M'), but we later augmented these with additional models with mass enhancement factors equal to 1 and 2 (models labelled 'R'). We also examined two models where we implemented a reduction in the corotation torques for protoplanets that develop eccentric orbits (discussed in detail in Sect.2.6). These models are labelled 'E'. Test calculations examining the influence of the planetesimal capture radii of protoplanets were also performed.

In order to ensure that the disc mass is locally comparable in models with different surface density profiles, we normalise the disc masses so that they all have the same mass in the region from 2-15 AU that the enhanced MMSN discs would have. This resulted in there being 28 protoplanets, with  $\sim 4200$  and  $\sim 2500$  planetesimals, for mass enhancement factors of 5 and 3, respectively. We limit our selection of the  $\alpha$  and  $\beta$  parameter space to models for which outward migration due to corotation torques is possible (the conditions for this can be determined by requiring the entropy-related and vorticity-related horseshoe drag terms in Sect. 2.6 to exceed the Lindblad torques). Our simulation parameters are detailed in Table 1.

We set an inner edge to our simulations at 1 AU, and any body that migrates inside this boundary, such that its semimajor axis is less than 1 AU, is removed from the simulation. Information, however, is stored about each body as it crosses this boundary, allowing us to follow the longer term trajectories of individual planets to determine their final stopping location as the gas disc disperses. This procedure is referred to as 'single-body analysis' later in the paper.

## 4 RESULTS

In this section we begin by describing common behaviour seen in many of the simulations. We introduce and discuss the concept of zero-migration lines, and their role in creating

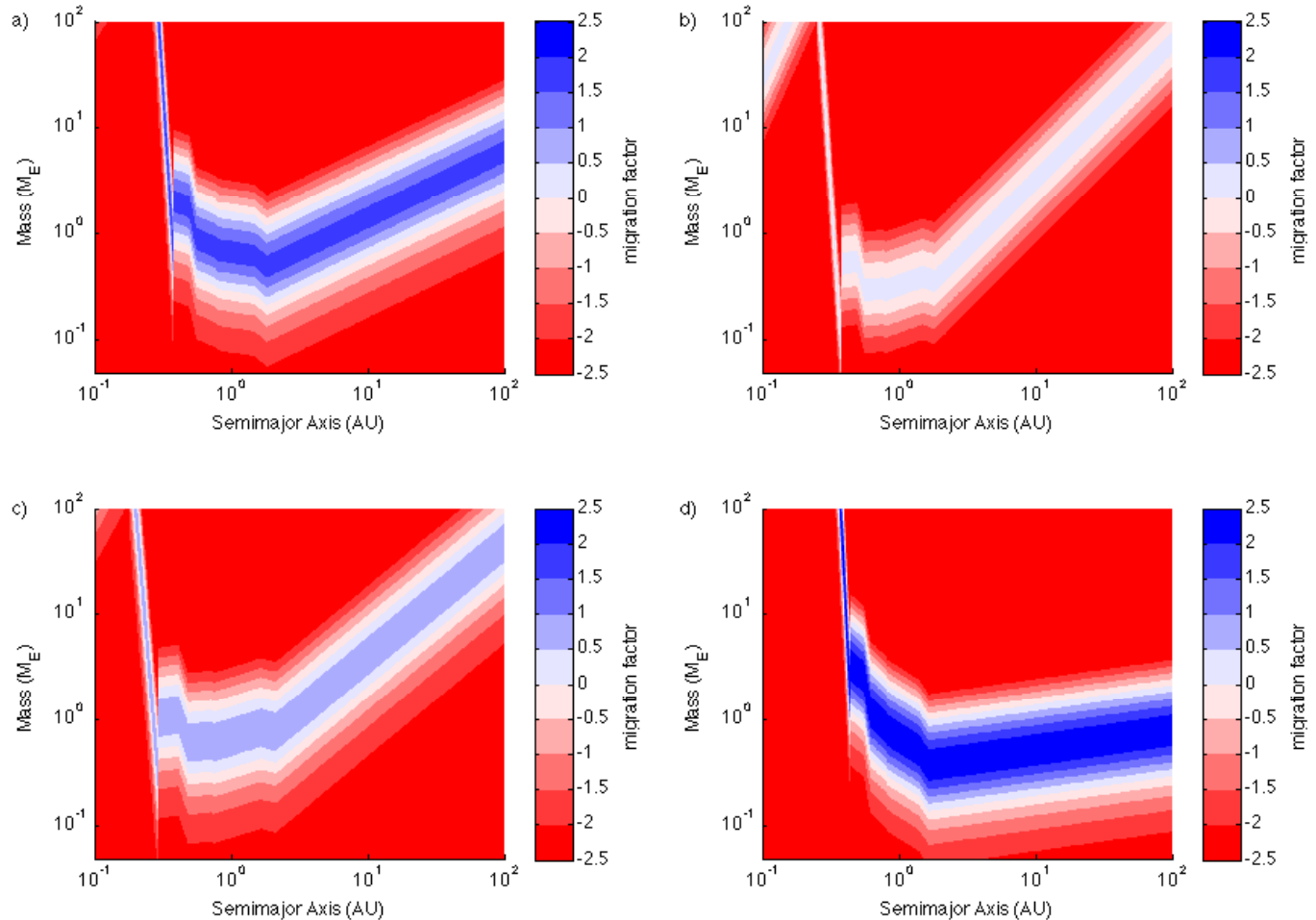


**Figure 3.** Contour plots showing regions of outward and inward migration in the mass–semimajor axis plane for runs M05A (a), M16A (b), M03B (c) and M07B (d).

convergent migration within a swarm of growing protoplanets. We also discuss the coupling between the mass growth of protoplanets and their migration, and how rapid accretion by protoplanets can lead to migration into the central star.

We then describe the detailed evolution of a selection of individual runs (four runs in total), followed by a summary of results across all of the simulations. This includes the results of single-body analyses, where we investigate the evolution of bodies lost beyond the inner edge of the simulations (these are treated as isolated bodies, and so the analyses are limited in their ability to provide accurate predictions about the nature of short-period systems).

Finally, we discuss briefly the effects of protoplanet eccentricity on the collective evolution of the system, and present results in which the strength of corotation torques is attenuated when a planet’s eccentric orbit induces a radial excursion that is larger than the horseshoe width.

Throughout this section, we define a gas giant as being a planet that has undergone runaway gas accretion, i.e. the sharp increase in mass shown in Fig. 2. This corresponds to a mass of approximately  $30 M_{\oplus}$ .

## 4.1 Common behaviour

### 4.1.1 Migration lines

Consider a planet orbiting in a protoplanetary disc with power-law surface density and temperature profiles. If the planet sits in the inner regions of the disc with high surface density and opacity, such that the horseshoe libration time is significantly *shorter* than the thermal/viscous diffusion time across the horseshoe region, then the corotation torques will saturate and be inoperable. The planet will migrate inward rapidly as its evolution will be determined by Lindblad torques.

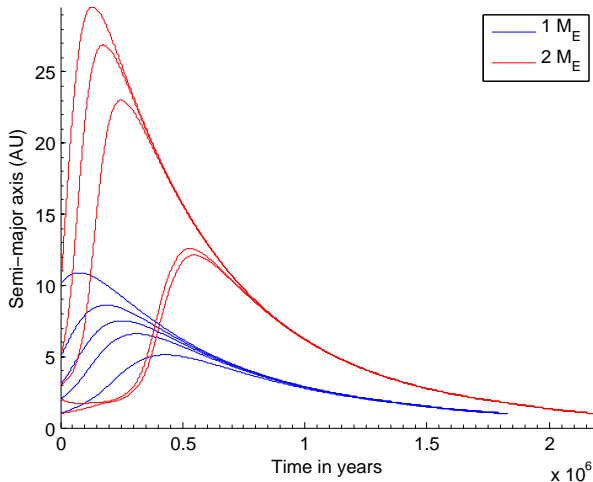
Consider the same planet orbiting much further out in the disc where the surface density and opacity are substantially reduced, such that the horseshoe libration time is much *longer* than the thermal/viscous diffusion time. The disc-planet system is now close to the locally isothermal limit, such that corotation torques will be close to their linear value (see Sect. 2.6). The migration will again be inward because of the dominance of the Lindblad torques, but at a reduced rate because of the contribution of positive corotation torques.

There exists an intermediate radial location in the disc where the surface density and opacity allow the ther-

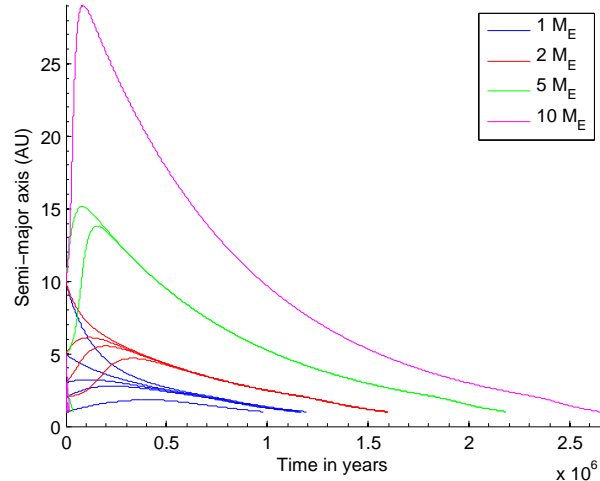


**Table 1.** Simulation parameters.

Simulation	$f_{\text{enh}}$	$\alpha$	$\beta$	$M_{\text{solid}}$	$a_{\text{snow}}$
M01A, M01B	5	0.5	0.75	173	1.95
M02A, M02B	3	0.5	0.75	104	1.95
M03A, M03B	5	0.5	1	173	1.65
M04A, M04B	3	0.5	1	104	1.65
M05A, M05B	5	0.5	1.25	173	1.49
M06A, M06B	3	0.5	1.25	104	1.49
M07A, M07B	5	0.5	1.5	173	1.39
M08A, M08B	3	0.5	1.5	104	1.39
M09A, M09B	5	0.75	1	173	1.65
M10A, M10B	3	0.75	1	104	1.65
M11A, M11B	5	0.75	1.25	173	1.49
M12A, M12B	3	0.75	1.25	104	1.49
M13A, M13B	5	0.75	1.5	174	1.39
M14A, M14B	3	0.75	1.5	104	1.39
M15A, M15B	5	1	1.25	170	1.49
M16A, M16B	3	1	1.25	107	1.49
M17A, M17B	5	1	1.5	170	1.39
M18A, M18B	3	1	1.5	107	1.39
M19A, M19B	5	1.25	1.5	173	1.39
M20A, M20B	3	1.25	1.5	104	1.39
R01A, R01B	2	0.5	1.25	69.6	1.49
R02A, R02B	1	0.5	1.25	36.6	1.49
R03A, R03B	2	0.5	1.5	69.6	1.39
R04A, R04B	1	0.5	1.5	36.6	1.39
R05A, R05B	2	0.75	1.25	69.6	1.49
R06A, R06B	1	0.75	1.25	36.1	1.49
R07A, R07B	2	0.75	1.5	69.6	1.39
R08A, R08B	1	0.75	1.5	36.1	1.39
E01A, E01B	5	0.5	1.25	173	1.49
E02A, E02B	3	0.5	1.25	104	1.49

**Figure 4.** Migration lines showing convergent behaviour for 1 and 2  $M_E$  planets in a disc with initial conditions as in M05A.

mal/viscous diffusion time to be approximately equal to the horseshoe libration time. The corotation torque (horseshoe drag) will be close to its maximum value here, and will possibly drive strong outward migration of the planet if the entropy gradient in the disc is steep enough. As the planet migrates outward, however, the local disc surface density and opacity decrease, decreasing the thermal diffusion time, and reducing the efficacy of the positive corotation torque. Eventually the planet reaches a location where the corotation and

**Figure 5.** Migration lines showing convergent behaviour for planets with varying mass in a disc with initial conditions as in M03B.

Lindblad torques exactly cancel, such that the planet stops migrating. We refer to this location as the zero-migration line, and these are stable positions in the disc for planets to reside.

Given that the horseshoe libration time is shorter for more massive planets, the zero-migration lines of heavier planets are located further out in the disc where the thermal diffusion times are shorter. Heavier planets that form in inner disc regions will need to migrate out past lower mass bodies to reach their zero-migration lines, leading to convergent migration for protoplanets with different masses. Furthermore, protoplanets with the same mass try to migrate to the same location in the disc. In principle, this should increase the rate of collisional planetary growth.

The behaviour described above is illustrated in the contour plots shown in Fig. 3, which display the value of the total torque in units of  $\Gamma_0/\gamma$  (defined in Eq. 19), as a function of planetary mass and orbital position. The four panels correspond to the initial models M05A, M16A, M03B and M07B that are described in Table 1. Regions coloured red correspond to strong inward migration (migration dominated by Lindblad torques). Regions coloured dark blue correspond to strong outward migration, and lightly coloured regions correspond to slow or zero migration. In general, rapid outward migration is favoured in discs with relatively flat surface density profiles and steep temperature profiles.

In a steady-state disc, a planet of fixed mass that migrates to its zero-migration line should stay there. Disc dispersal, however, leads to a locally reducing surface density and opacity, progressively shifting the zero-migration line inward. Consequently, as the disc disperses, a planet sitting on a zero-migration line drifts inward on the gas disc dispersal time scale. This behaviour is shown in Figs. 4 and 5, which show the migration trajectories of planets of different mass in the two disc models M05A and M03B that are dispersing on time scales of 1 Myr (similar migration trajectories are shown in Lyra, Paardekooper, & Mac Low (2010)). Planets of a given mass starting at different locations tend to migrate outward and eventually join the same migration line, which then moves inward as the disc disperses. The behaviour of

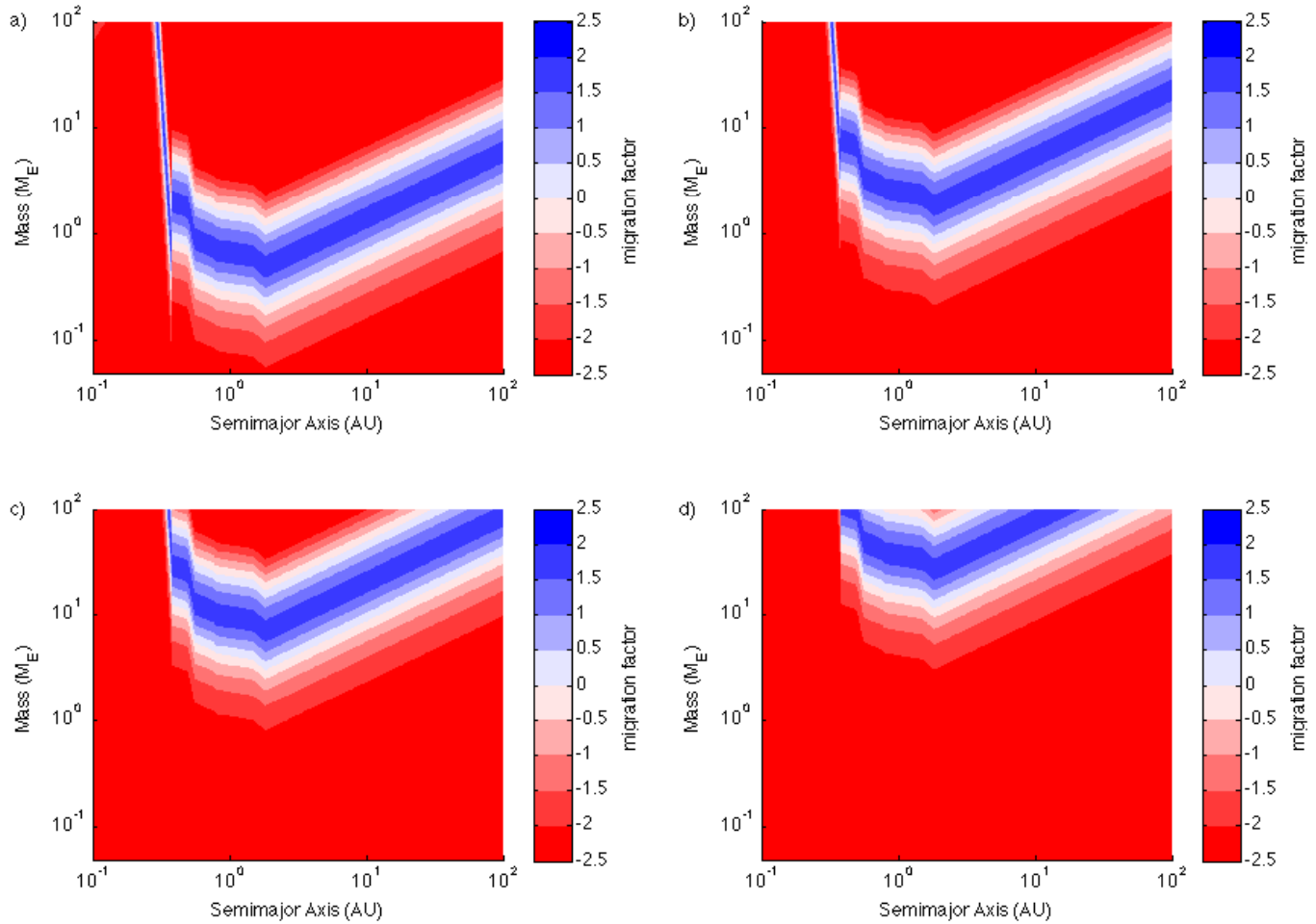


**Figure 6.** Contour plots showing regions of outward and inward migration for run M05A at  $t=0$  years (a),  $t=1,000,000$  years (b),  $t=2,000,000$  years (c) and  $t=3,000,000$  years (d).

the contours shown in the top left panel of Fig. 3 under the action of disc dispersal are shown in Fig. 6. It is clear that as the disc becomes increasingly optically thin, only heavy planets can sustain outward migration (unless they become too massive and enter the type II migration limit because of gap formation).

#### 4.1.2 Influence of mass growth

A planet undergoing mass growth while sitting on a zero-migration line should migrate outward as it accretes, since zero-migration lines for heavier planets lie at larger distances from the central star. However, if the mass growth rate of the planet exceeds the outward migration rate due to corotation torques, then a very different fate awaits it. Consider a planet of mass  $\sim 0.5 M_{\oplus}$  sitting at  $\sim 2$  AU in the top left panel of Fig. 6. Rapid growth of the planet up to  $10 M_{\oplus}$  in less than 1 Myr will put the planet in the regime of rapid inward migration, as its trajectory in the figure will be almost vertical, moving it out of the blue region and into the red one. Very rapid growth of planets, therefore, may not lead to strong outward migration but instead may cause planets to migrate rapidly into the central star. The timing of the

growth of planets is crucial in determining their long-term survival.

## 4.2 Individual runs

### 4.2.1 Run M05A

Run M05A has an initial disc mass equivalent to 5 times the MMSN,  $\alpha = 0.5$  and  $\beta = 1.25$ . The magnitude and sign of migration torques ( $t = 0$ ) are shown in the top left panel of Fig. 3, and the effects of disc dispersal are demonstrated in Fig. 6. It is clear that planets with masses in the range  $0.2 \leq m_p \leq 1 M_{\oplus}$ , initially located in the disc region  $1 - 10$  AU, can undergo strong outward migration. Growth of planets to masses of a few  $M_{\oplus}$  may lead to outward migration over distances of tens of AU.

The time evolution of planet masses (top panel), semi-major axes (middle panel) and eccentricities (bottom panel) are shown in Fig. 7. During the first 0.3 Myr, we observe that three planets grow in mass rapidly, and undergo outward migration to  $\sim 10$  AU. The mass growth occurs as a result of planetesimal accretion and planet-planet inelastic collisions, and the rapid growth is assisted by convergent migration within the protoplanet swarm and by the gas envelopes that form within the planet Hill spheres. When the planet masses

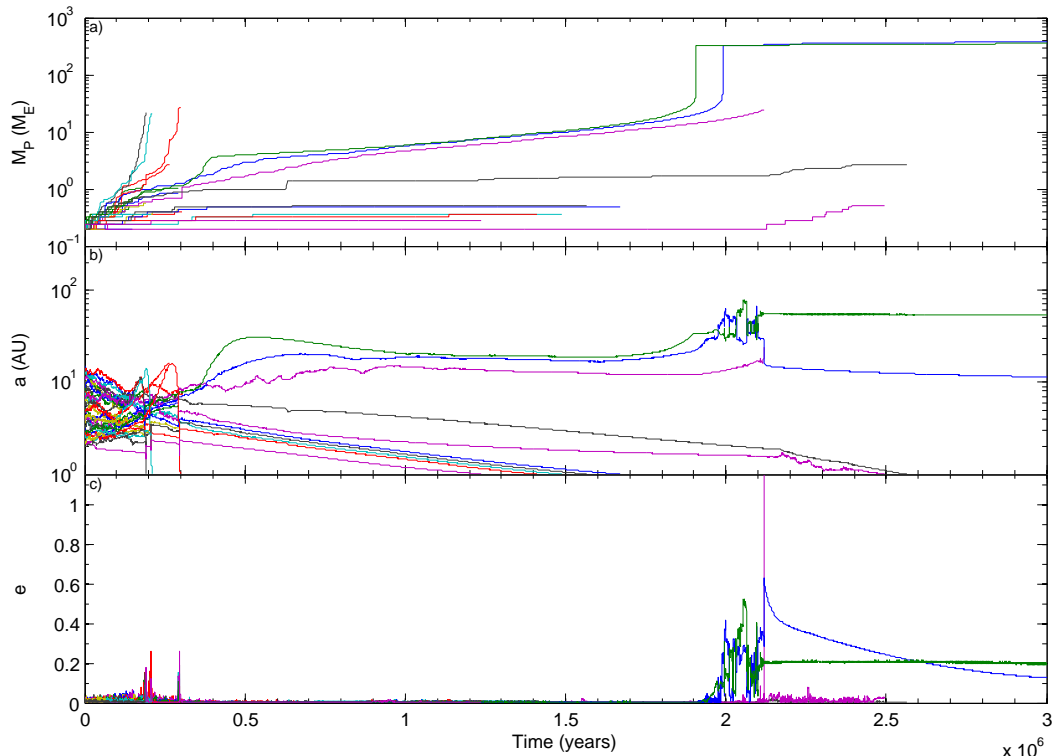


**Figure 7.** Evolution of the masses, semimajor axes and eccentricities of all protoplanets simulation M05A.

exceed  $\sim 20 M_{\oplus}$ , however, their migration direction changes and they undergo very rapid inward migration through the planetary swarm and interior to 1 AU, the inner boundary of the simulation. During the rapid inward migration, there is very little accretion by these bodies, but they temporarily excite the eccentricities of the other bodies in the system (see the bottom panel of Fig. 7 between 0.2 – 0.3 Myr).

Between the times 0.3 – 0.5 Myr, we observe that three bodies grow to masses larger than  $1 M_{\oplus}$ . The largest of these grows to  $\sim 4 M_{\oplus}$  and migrates outward rapidly to  $\sim 30$  AU, the location of its zero-migration line. We refer to this as “planet A”. A second planet (“planet B”) grows to a mass  $\sim 3 M_{\oplus}$  by 0.5 Myr, and migrates out to its zero-migration line at  $\sim 20$  AU. A third planet (“planet C”) reaches a mass of  $\sim 2 M_{\oplus}$  at 0.5 Myr and migrates out to 10 AU. Although the protoplanet/planetesimal disc of solids is truncated at 15 AU in the initial simulation set-up, outward migration of planets and gravitational scattering transports planetesimals into the outer disc where they are accreted by planets A and B (planet C continues to reside within the original planetesimal disc). Gas accretion ensues once these bodies exceed  $3 M_{\oplus}$ , and we see their masses grow smoothly up to  $20 - 30 M_{\oplus}$  between the times 0.5 – 2 Myr. During this time the zero-migration lines move inward (observe the modest inward migration in the middle panel of Fig. 7 between 0.5 – 2 Myr), but continued mass growth helps to counterbalance this effect, and prevents substantial inward migration. At approximately 2 Myr, planets A and B undergo rapid gas accretion and grow to become Jovian-mass giant planets (further gas accretion occurs at the viscous-supply rate). The rapid mass growth induces dynamical instability between planets A and B, causing them to undergo a period

of gravitational scattering and eccentricity growth (bottom panel of Fig. 7). The scattering eventually causes planets B and C to collide at 2.1 Myr (when planet C has a mass of  $24 M_{\oplus}$ ), leaving two giant planets on eccentric, non-crossing orbits with semimajor axes of 12 and 55 AU. The inner planet has a total mass of  $374 M_{\oplus}$ , and a solid core mass of  $27.6 M_{\oplus}$ , at the end of the simulation. The outer planet has a total mass of  $352 M_{\oplus}$ , and a solid core mass of  $10.1 M_{\oplus}$ .

During the formation of the outer gas giant planets, between time 0.5 – 2.5 Myr, only modest planetary growth occurs in the inner system. An inner resonant convoy, similar to those discussed by McNeil, Duncan, & Levison (2005) and Cresswell & Nelson (2006) migrates interior to 1 AU by  $\sim 1.6$  Myr, driven by a more rapidly migrating  $0.5 M_{\oplus}$  body. This leaves behind two planets that grow to become  $\sim 3$  and  $0.4 M_{\oplus}$  before migrating interior to 1 AU at  $\sim 2.5$  Myr.

#### 4.2.2 Run M16A

Run M16A has a disc mass equivalent to 3 times the MMSN,  $\alpha = 1$  and  $\beta = 1.25$ . The migration behaviour at  $t = 0$  is illustrated by the contours displayed in the top right panel of Fig. 3, and it is clear that outward migration is considerably weaker in this model than in the previously described run M05A. Furthermore, the steepness of the outward migration region as one moves to higher planet masses indicates that the radial extent of outward migration is also reduced relative to model M05A. Placed in the initial disc model, a planet with  $m_p < 1 M_{\oplus}$  orbiting at 1 AU will not undergo outward migration at all, but will instead migrate inward only. Rapid planetary growth is therefore expected to result

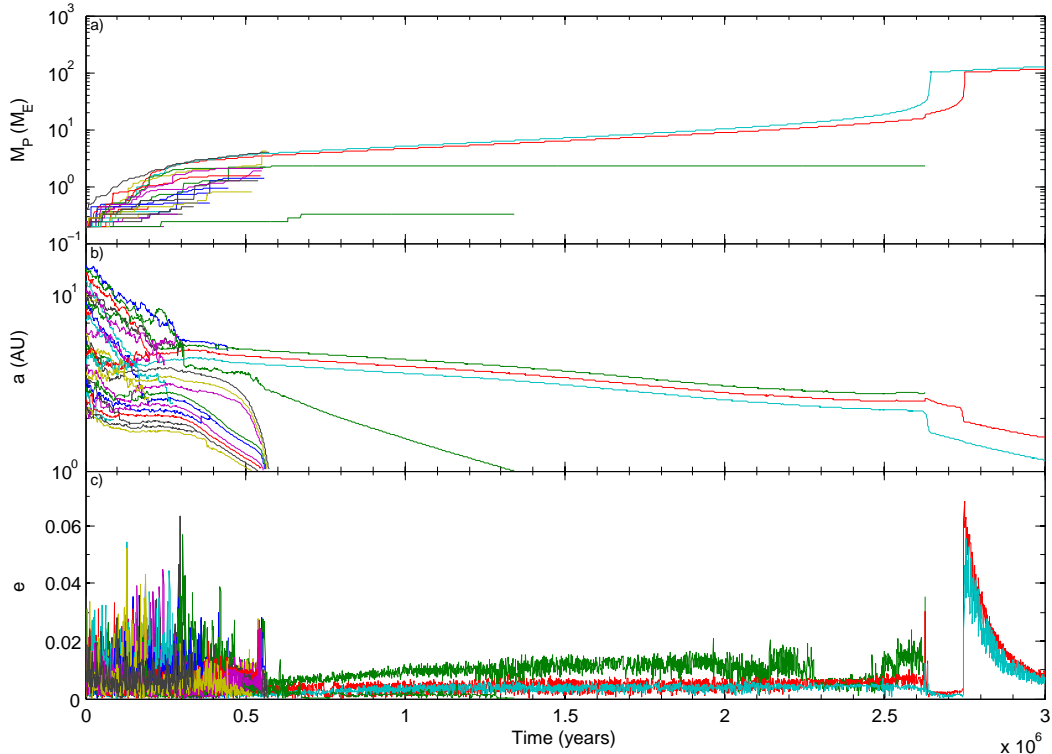


**Figure 8.** Evolution of the masses, semimajor axes and eccentricities of all protoplanets in simulation M16A.

in much of the solid disc material migrating in toward the star.

The evolution of the planetary masses (upper panel), semimajor axes (middle panel) and eccentricities (bottom panel) are shown in Fig. 8. Protoplanets located initially beyond  $\sim 2$  AU in this disc with masses  $\simeq 0.02 M_{\oplus}$  (the initial masses of protoplanets in the model) are expected to migrate inward, and looking at the middle panel of Fig. 8 we see obvious evidence for this migration occurring within the first 0.3 Myr. Looking at the inner part of the system during the first 0.5 Myr, we observe two examples of resonant, inward migrating convoys being established. The first to form consists of the six innermost protoplanets in the system. All masses of these planets are  $< 1 M_{\oplus}$ , except for the outermost body, whose mass has grown to  $\sim 1 M_{\oplus}$ . The more rapid migration of this body drives the inward migration of the whole convoy. At a time of  $\sim 0.4$  Myr, we see that the next three nearest protoplanets to the central star begin to undergo rapid inward migration, and this is driven by the formation of a  $\sim 5 M_{\oplus}$  body whose progenitor protoplanet was located at  $\sim 4$  AU. The growth of this protoplanet induces rapid inward migration, with the system of inner planets being swept interior to 1 AU at  $t = 0.55$  Myr.

Three planets initially located at  $\sim 5$  AU become physically detached from the rest of the system after  $\sim 0.5$  Myr, as shown in the middle panel of Fig. 8. These bodies have all grown to masses between  $2 - 5 M_{\oplus}$  within this time. The outermost  $\sim 2 M_{\oplus}$  body becomes isolated from planetesimals in the disc such that its mass does not grow after 0.5 Myr. This isolation occurs in large part because the two more massive neighbouring planets accrete the nearby planetesimals. Having achieved masses in excess of  $3 M_{\oplus}$ , these

two planets are able to accrete gas. As they do so, they sit on their zero-migration lines and undergo slow inward migration, where the speed of migration is attenuated by the continuing gas accretion and mass growth (the planets try to migrate outward to the zero-migration lines for more massive planets as they grow, at the same time as the zero-migration lines move inward as the gas disc evolves). After  $\sim 2.6$  Myr, the innermost planet reaches a mass of  $\sim 30 M_{\oplus}$  and undergoes rapid gas accretion to become a Saturn-mass gas giant. The rapid mass growth dynamically disturbs the system, as observed in the middle and bottom panels of Fig. 8, causing the outer  $2 M_{\oplus}$  planet to collide with the middle planet. Shortly after, this merged planet undergoes rapid gas accretion to also become a Saturn-mass gas giant. Saturnian rather than Jovian masses are achieved because accretion occurs late in the disc lifetime, such that the gas isolation mass limits the envelope mass to  $\sim 100 M_{\oplus}$ .

At the end of the simulation we have an inner planet of total mass  $115 M_{\oplus}$ , with solid core mass  $11 M_{\oplus}$ , orbiting at 2.3 AU, and an outer planet with total mass  $127 M_{\oplus}$ , solid core mass  $8.8 M_{\oplus}$ , orbiting at 3.1 AU.

#### 4.2.3 Run M03B

Run M03B has a disc mass equivalent to 5 times that of the MMSN,  $\alpha = 0.5$  and  $\beta = 1$ . The migration behaviour of this model at  $t = 0$  is illustrated by the lower left panel in Fig. 3, showing that this disc is intermediate between the two previous models discussed (M05A and M16A) in terms of the strength of outward migration.

The evolution of the planetary masses (upper panel), semimajor axes (middle panel) and eccentricities (bottom

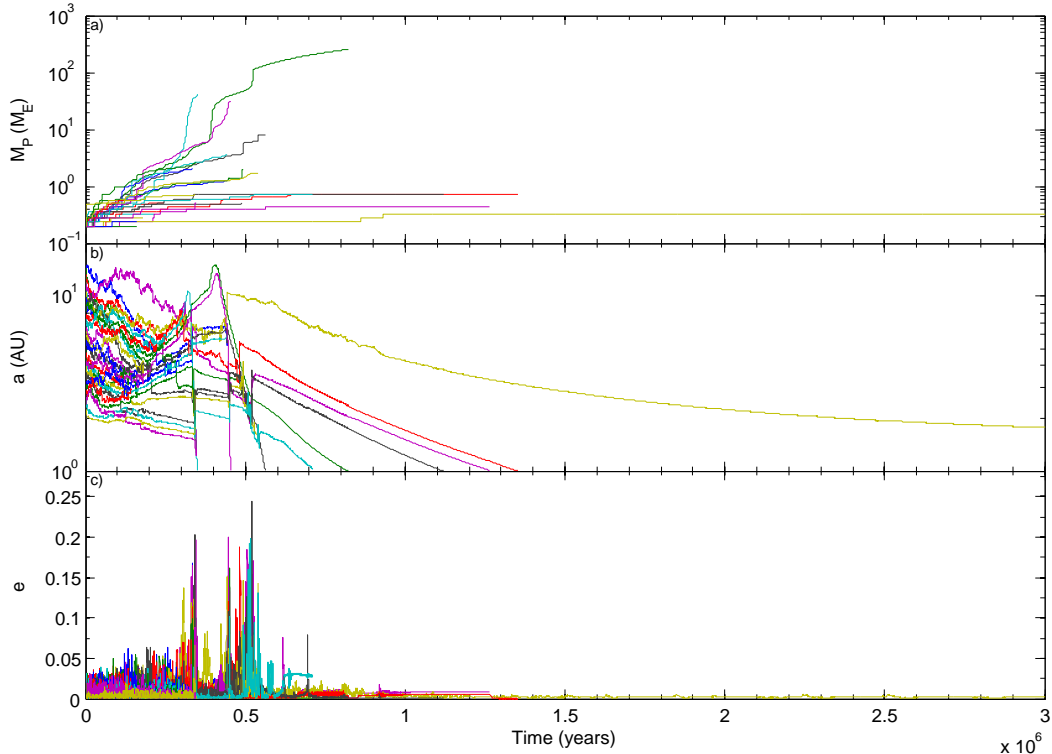


**Figure 9.** Evolution of the masses, semimajor axes and eccentricities of all protoplanets in simulation M03B.

panel) are shown in Fig. 9. As expected from comparing the migration behaviour of the runs M16A and M03B in Fig. 3, the initial stages of run M03B show some similarities to run M16A. Protoplanets initially located in the region of the protoplanet/planetesimal disc between 10 – 15 AU migrate inward to the region centred around 2 – 3 AU. The inner planets, however, do not show a strong tendency to migrate inward (differing in this regard from run M16A), and the convergent migration stimulates substantial growth within the protoplanet swarm, as seen in the upper panel of Fig. 9, where the planet masses are seen to increase during the first 0.5 Myr, and in the middle panel where it is clear that collisional growth reduces the number of planets. The strong planetary growth, however, also leads to rapid inward migration. Bodies that reach masses in excess of  $20 M_{\oplus}$  undergo rapid inward migration through the disc of protoplanets/planetesimals and interior to 1 AU, exciting the eccentricities of the remaining planets as they do so. The bodies that rapidly migrate through the inner boundary at 1 AU would hit the star if their long-term evolution were followed.

One of the quickly migrating planets (shown by the upper green line in the top panel of Fig. 9) grows to be massive enough (approximately  $30 M_{\oplus}$  of solids) to undergo rapid gas accretion during the inward migration. It reaches its gas isolation mass at a mass equal to  $114 M_{\oplus}$ , and transitions to type II migration, drifting interior to 1 AU shortly after 0.8 Myr has elapsed. At this point in time, the planet mass is  $\sim 250 M_{\oplus}$ , and it is undergoing gas accretion from the disc at the viscous-supply rate. We have followed the evolution of this body after it has traversed the inner boundary of the simulation, treating it as an isolated body and neglecting

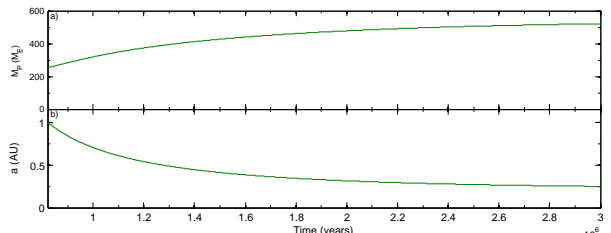


**Figure 10.** Evolution of mass and semimajor axis of single body extension run for the hot Jupiter in simulation M03B starting at 0.821 Myr.

its interaction with other bodies in the system (we refer to this as single-body analysis). The evolution is displayed in Fig. 10, and we see that the planet reaches a semimajor axis of 0.25 AU and has a mass of  $524 M_{\oplus}$  after 3 Myr, making it an excellent candidate for a hot Jupiter.

No other planets grow substantially during the evolution of this run. Fig. 9 shows that only a single planet with mass  $\sim 0.35 M_{\oplus}$  survives beyond 1 AU, coming to rest at a semimajor axis of  $\sim 1.9$  AU.

#### 4.2.4 Run M07B

The final run we describe in detail is M07B, which has a mass equivalent to 5 times the MMSN,  $\alpha = 0.5$  and  $\beta = 1.5$ . The steep temperature gradient and relatively shallow surface density gradient allow this disc model to support strong outward migration over a large radial extent, as illustrated by the contours in the bottom right panel of Fig. 3. This plot demonstrates clearly that sub-Earth mass bodies orbit-

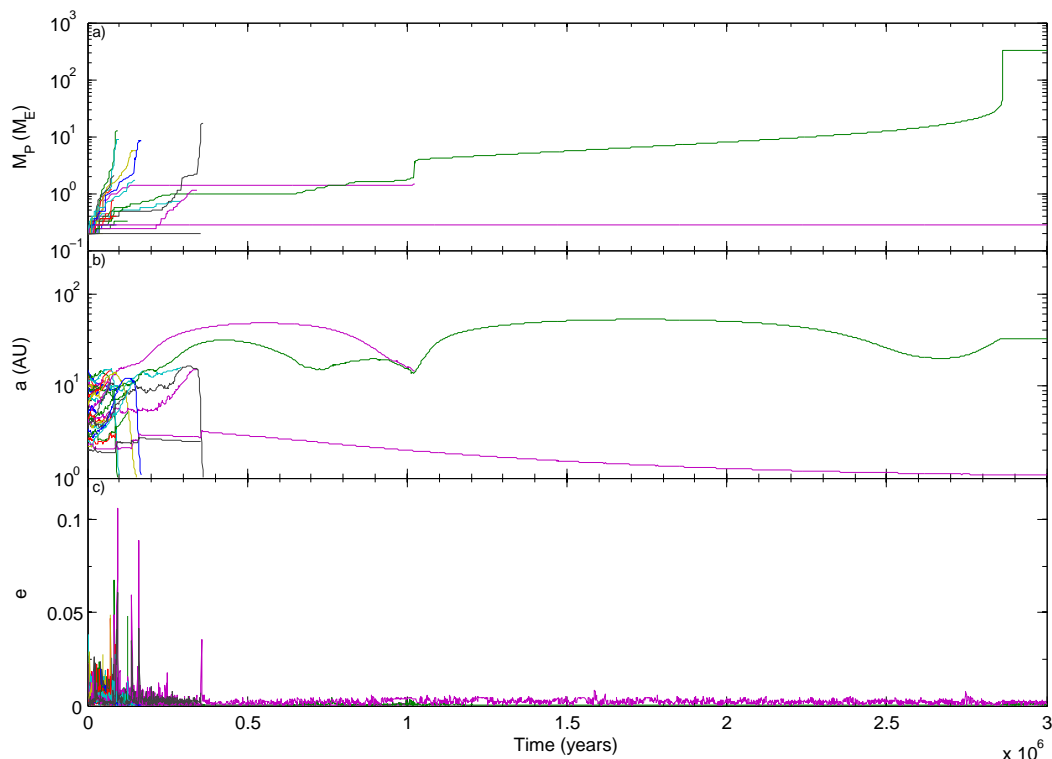


**Figure 11.** Evolution of masses, semimajor axes and eccentricities of all protoplanets in simulation M07B.

ing in the vicinity of 1 AU will experience strong outward migration, possibly out beyond 100 AU.

The evolution of planetary masses (top panel), semi-major axes (middle panel) and eccentricities (bottom panel) are shown in Fig. 11. The initial growth and outward migration of protoplanets in the inner region of the swarm leads to strongly convergent migration, and rapid growth of a number of bodies up to  $\sim 10 M_{\oplus}$  within the first 0.3 Myr. As observed in the previously described runs, this leads to rapid inward migration of these planets because the horseshoe libration time becomes much shorter than the thermal/viscous diffusion time for these bodies. After 0.5 Myr, there are only three bodies left in the simulation: two planets orbiting at  $\sim 15$  AU each with masses  $\sim 2 M_{\oplus}$ ; one protoplanet with mass  $\sim 0.3 M_{\oplus}$  orbiting at  $\sim 2$  AU. The two outer bodies collide shortly after 0.5 Myr, and the resulting planet undergoes slow gas accretion, migrating outward as it does so. After 2.8 Myr it undergoes rapid gas accretion and becomes a Jovian mass ( $319 M_{\oplus}$ ) gas giant planet, with a  $5.2 M_{\oplus}$  solid core, orbiting at  $\sim 33$  AU. As in model M05A, we find that gas giant planets can be formed at large radius from the central star by the migration and gas accretion onto a solid core. In both of these models (and others not discussed in detail), the mode of formation is one in which an initial generation of massive protoplanets form and migrate in toward the central star, followed by a second generation of more isolated lower mass cores that can migrate out slowly and accrete gas at the same time. Such a model may provide a natural explanation for the massive planets orbiting at large distance from their host stars, such as HR 8799 (Marois et al. 2010), Fomalhaut (Kalas et al.

2008), and Beta Pictoris (Lagrange et al. 2010), that are being discovered by direct imaging surveys.

### 4.3 Summary of all runs

We ran 40 simulations with  $f_{\text{enh}} = 5$  or 3, surface density power-law indices in the range  $0.5 \leq \alpha \leq 1.25$ , and temperature power-law indices satisfying  $0.75 \leq \beta \leq 1.5$ . In total 19 gas giant planets were formed in these runs, and their properties are summarised in Fig. 12 and Table 2. The giant planet masses range from 115 to  $670 M_{\oplus}$ , and have solid core masses in the range  $3.6 - 39 M_{\oplus}$ . Looking at the upper panel of Fig. 12, we see that most giant planets are grouped within the mass range 320 to  $400 M_{\oplus}$ , and this is very likely to be an artifact of our gas accretion procedure that limits the planet mass obtained during rapid gas accretion to be the Jovian mass. A more sophisticated procedure would be sensitive to local conditions in the disc, and result in a broader spread of planet masses, and this is clearly one future improvement that we will need to implement in our modelling procedure. Nonetheless, we do also obtain giant planets outside of this mass range. Run M03B formed a  $523.8 M_{\oplus}$  planet, as discussed in Sect. 4.2.3, due to a gas giant forming within the first 0.5 Myr, and subsequently accreting viscously and migrating via type II migration to its final location at 0.25 AU. The heaviest planet formed during run M11A, and this was the result of two gas giant planets colliding, having each formed at between 20 and 30 AU from the central star due to their cores migrating outward. Employing a pure hit-and-stick prescription for planetary collisions, however, probably leads to an overestimate of the final mass of this planet. Three planets were formed with masses



below the imposed Jovian-mass limit. Run M12B produced a  $296 M_{\oplus}$  planet orbiting at 9.8 AU, and as described in Sect. 4.2.2, run M16A produced a pair of Saturn-mass objects orbiting at 1.15 and 1.55 AU. These planets formed late in the disc lifetime, such that their gas isolation masses were below the Jovian mass.

Most of the giant planets formed at semimajor axes substantially beyond 10 AU. Indeed, only 4 out of 19 giant planets formed interior to 10 AU. The reason for this is that the most common mode of gas giant planet formation in the simulations was the formation of a core of modest mass in the interior disc, that then migrates outward over large distances before accreting a gas envelope. Many massive cores formed during the early stages of the disc life times in the simulations, and were able to undergo gas accretion. Their rapid inward migration, however, prevented them from surviving. Giant planets that form closer to the star and survive tend to be in disc models (M03B and M16A) that generate weaker corotation torques.

There are three simulations that lead to the formation of surviving multiple giant planets. Run M05A produces a pair of Jovian mass planets orbiting at 11.4 and 53.9 AU, as described in Sect. 4.2.1, and M05B also produced a pair of Jovian mass objects orbiting at 23.3 and 68.8 AU. Note that these runs were identical apart from the random number seed used to generate initial conditions. Run M16A produced a pair of Saturn-mass planets orbiting at 1.15 and 1.55 AU. One consequence of this is that almost all giant planets formed in the simulations are on circular, non-inclined orbits. The only planets with significant eccentricities are those in run M05A, where gravitational scattering during the formation caused the growth of eccentricity.

One surprising result to come out of the simulations is the lack of correlation between initial disc mass and the frequency of giant planet formation. Discs with  $f_{\text{enh}} = 5$  formed 9 giants and those with  $f_{\text{enh}} = 3$  formed 10. This led us to question whether less massive discs might be able to form gas giants. To examine this, we performed additional simulations (labelled ‘R’ in Table 1) based on the most successful models in the  $f_{\text{enh}}=3$  and 5 runs. All barring one failed to produce any gas giants. Run R07B, a  $f_{\text{enh}}=2$  disc, did produce a single Jovian mass gas giant (shown in Fig. 12).

In addition to the giant planets discussed above, the simulations also resulted in the formation and survival of lower mass bodies beyond 1 AU in the disc. These are shown in Fig. 13. The rapid growth of cores, followed by rapid inward migration, has the effect of clearing much of the solid material from beyond 1 AU, and the outward migration of modest sized cores that evolve into gas giants also clears this region. Nonetheless, terrestrial mass bodies do form and survive in the simulations, although Fig. 13 shows that these tend to be in the lower mass discs. One noticeable and interesting observation about the simulation results is the lack of super-Earth and Neptune mass planets. The rapid formation of massive cores that undergo fast inward migration is a major cause of this (driven by efficient capture of planetesimals and convergent migration), but a contributing factor is the fact that planets with masses greater than  $3 M_{\oplus}$  can begin to undergo gas accretion in our models. A higher threshold for gas accretion would probably allow some of the giant planets that formed to have maintained lower masses. These observations provide a useful guide to the types of

modifications that the modelling procedure requires in order to form planets with the same characteristics as those which are contained in the extrasolar planet observational database.

#### 4.3.1 Single-body analysis

The inner edge of our simulations was set at 1 AU. We ran single body runs for each object that was lost beyond this inner edge so as to identify any bodies that would have become short period gas giants, and to obtain an estimate of the distribution of smaller bodies in this inner region. These runs are effectively continuation runs, but with a smaller time step size, and a smaller inner boundary at 0.1 AU. It is important to note that these single body runs did not include the influence of any other planets in the system, and did not account for any material that would have been present between 0.1 – 1 AU during the early evolution of the system. As such, the results merely provide a guide to the planets that can survive within this radial range.

Figure 14 shows a summary of all non-giant planets left remaining in the 0.1 to 1 AU region from all the  $f_{\text{enh}}=3$  and 5 models. Objects with masses less than  $1 M_{\oplus}$  are clearly more common than those with larger masses because of their reduced migration rates. Also, smaller semimajor axes seem the more likely outcome. All objects included in this figure have masses below  $3 M_{\oplus}$  and have not been able to undergo gas accretion. The only gas giant to survive in the region 0.1 – 1 AU is the one described already in Sect.4.2.3.

A large number of bodies are lost beyond 0.1 AU, ranging from the smallest protoplanets all the way up to Jupiter sized gas giants, potentially providing the central star with a significant enrichment of heavy elements. These bodies are summarised in Fig. 15, which shows the masses of the planets as they cross the boundary at 1 AU in the lower panel, and their masses as they cross the boundary at 0.1 AU in the upper panel. The horizontal axes show the time of loss through the boundary at 0.1 AU. It is clear that a number of the massive cores that migrate through the 1 AU boundary accrete gas and become gas giants, although their masses normally reach values between  $100 - 200 M_{\oplus}$  because the gas isolation mass is below the Jovian-mass in the inner disc. Type II migration drives them through the boundary at 0.1 AU. It is also clear that a number of bodies migrate inside 1 AU with masses in the range  $4 - 10 M_{\oplus}$  and grow through gas accretion to masses between  $30 - 50 M_{\oplus}$ . Type I migration, however, forces these bodies to migrate into the star before they can become giants. Their corotation torques are saturated, and so rapid inward migration is driven by Lindblad torques.

Some of the bodies passing through the 0.1 AU boundary at late times could have survived. We ran extended single body runs for the five planets with masses greater than  $25 M_{\oplus}$  lost beyond 0.1 AU in the last 500,000 years of simulation time. Two collided with the central body at 2.75 Myr, but the other three survived at 0.086, 0.0428 and 0.016 AU with masses 344, 164 and  $550 M_{\oplus}$ , respectively. We have not included these results along with the other gas giants since their simulation conditions were overly simplified compared to the rest. All three bodies entered the 1 AU zone with just a few Earth masses, and so would in reality have interacted with other bodies and planetesimals formed there

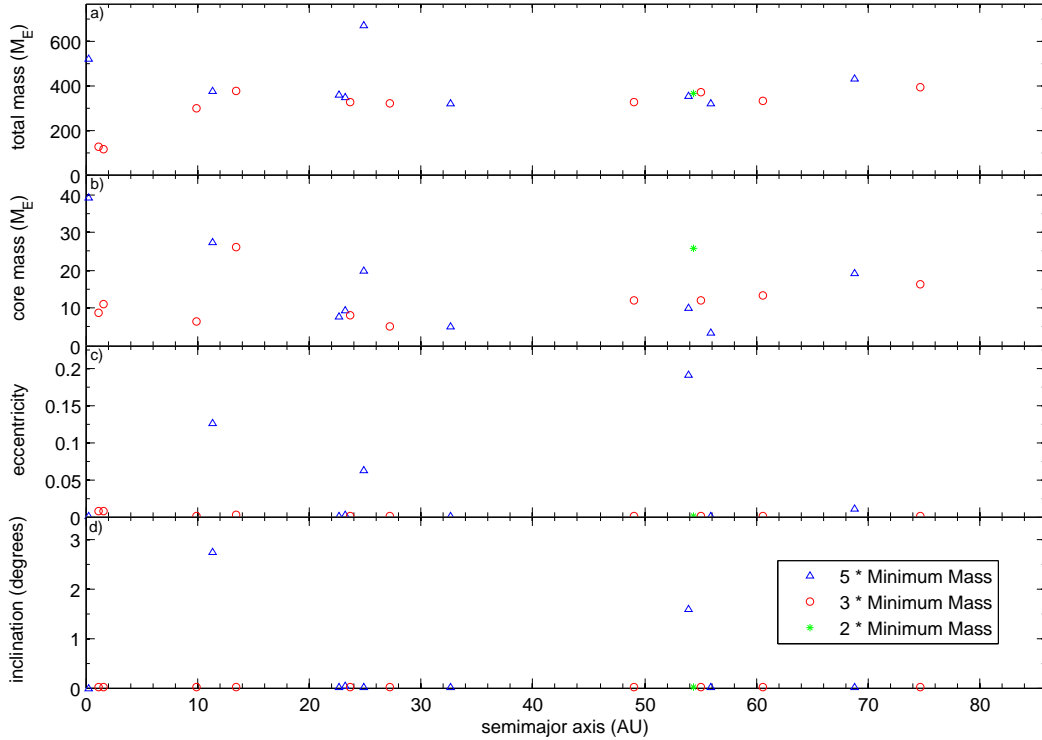


**Figure 12.** Summary of total masses, core masses, eccentricity and inclination against semimajor axis for all gas giant planets formed.

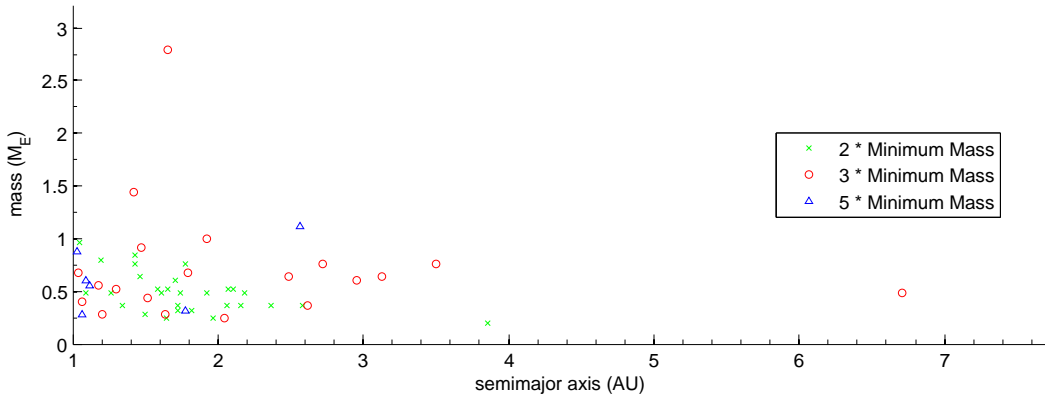


**Figure 13.** Summary of masses against semimajor axis for all small surviving planets outside 1 AU.

which were not modelled. Also, the body ending up at 0.016 AU would most likely have been accreted by the central star a short while later.

The survivability of these giant planets formed in single body analyses between 1 and 0.1 AU depends on exactly how the gas disc dissipates. The exponential dissipation of gas provides a reasonable approximation for the bulk of the gas dissipation when it is dominated by viscous evolution (Fogg & Nelson 2007), but at later times the structure of a viscously evolving disc that is being photoevaporated by UV radiation from the central star changes substantially (Clarke, Gendrin, & Sotomayor 2001) with a low density inner cavity being formed. Clearly such a model needs to be incorporated into the simulation procedure outlined here to

make reasonable predictions about the nature of surviving short-period planets.

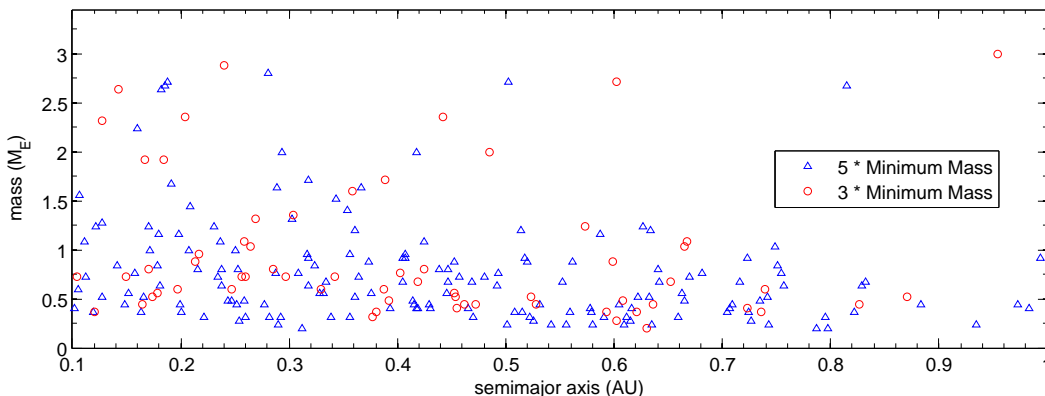
#### 4.4 Eccentricity modulation of corotation torques

Recent numerical simulations (Bitsch & Kley 2010) indicate that corotation torques are substantially reduced in their effectiveness when a planet develops an eccentric orbit. In particular, we expect the corotation torque to be effectively quenched when the radial excursion associated with the eccentric orbit exceeds the width of the horseshoe region. In order to simulate this effect, we have run a few simulations (labelled 'E' in Table 1) where the eccentricity modulation function in Eq. 21 is switched on. The effect of this was as one might expect: growth was significantly stunted com-



**Table 2.** Summary of gas giants formed.

Simulation	$f_{\text{enh}}$	$\alpha$	$\beta$	a (AU)	e	i (degrees)	mass ( $M_{\oplus}$ )	core mass ( $M_{\oplus}$ )
M03B	5	0.5	1	0.24818	0.000001	0	523.79	39.39
M05A	5	0.5	1.25	11.39435	0.125762	2.7366	374.36	27.57
M05A	5	0.5	1.25	53.91049	0.191585	1.5949	352.2	10.11
M05B	5	0.5	1.25	23.26593	0.00314	0.0299	351.47	9.51
M05B	5	0.5	1.25	68.79704	0.011044	0.0195	433.61	19.18
M06A	3	0.5	1.25	54.99131	0.000684	0.0026	369.38	12.11
M06B	3	0.5	1.25	74.69739	0.000847	0.0012	392.5	16.1
M07A	5	0.5	1.5	55.91612	0.000897	0.0006	319.86	3.6
M07B	5	0.5	1.5	32.59897	0.00098	0.0057	319.24	5.19
M08A	3	0.5	1.5	13.41661	0.001873	0.0106	374.61	26.13
M08B	3	0.5	1.5	60.55699	0.000785	0.0021	333.38	13.35
M11A	5	0.75	1.25	24.93238	0.063072	0.0053	669.88	19.7
M11B	5	0.75	1.25	22.70169	0.000959	0.0069	361.13	7.79
M12B	3	0.75	1.25	9.87598	0.000726	0.0022	296.43	6.47
M14A	3	0.75	1.5	27.22201	0.000179	0.0046	323.17	5
M14B	3	0.75	1.5	49.00695	0.000497	0.0036	328.24	12.07
M16A	3	1	1.25	1.55415	0.008245	0.0008	114.91	10.9511
M16A	3	1	1.25	1.15495	0.007372	0.0008	126.85	8.8343
M18B	3	1	1.5	23.61206	0.000516	0.0111	325.91	7.95
R07B	2	0.75	1.5	54.41991	0.000599	0.0016	367.3	25.77

**Figure 14.** Summary of masses against semimajor axis for all small surviving planets interior to 1 AU. Note that these data were obtained using the single-body analysis described in the text.

pared to the corresponding runs without this reduction factor (runs M05A/B compare to eccentricity damping runs E01A/B and M06A/B compare to E02A/B). Nearly all protoplanets were lost beyond the inner edge by approximately 1 Myr and most protoplanets were lost within half this time. Only one planet survived to run completion out of all four of the simulations and its final position is shown in Fig. 18, which shows a summary of surviving planets from the ‘E’ runs, as well as those discussed below in which the enhanced planetesimal capture radii are switched off. A plot showing the time evolution of this particular simulation is given in Fig. 16, where we have plotted the eccentricity in the bottom panel as  $e/x_s$ . It is clear that planet-planet interactions maintain values of  $e/x_s \geq 1$  throughout the simulation, until it is depleted of planets through their inward migration. This result suggests that closer investigation of the role of planetary eccentricity in regulating the strength of corotation torques needs to be undertaken, since the modest evidence we have accumulated suggests that mutual encounters between planets may remove the benefits provided by corotation torques in enhancing the formation and survival of

planets. Similar conclusions have been reached in a recent study by McNeil & Nelson (In preparation) that examines the formation of hot Neptunes and super-Earth planets in radiatively inefficient discs.

#### 4.5 Capture radii enhancement switched off

A common outcome within our simulations has been the rapid formation and growth of planetary cores, and their subsequent rapid migration inward. One reason for this rapid growth is our adoption of an enhanced capture radius for planetesimals arising because of a putative gaseous envelope settling onto protoplanets during their formation. We re-ran the simulations described in Sect. 4.2 without enhanced capture radii. Growth was notably slower as expected in all four runs. Two runs, however, (corresponding to the M03B and M07B non-atmosphere runs) did manage to form one gas giant planet each.

The time evolution of run M03B-NA (non-atmosphere) is shown in Fig. 17. A planet grows slowly to just over  $3 M_{\oplus}$  by approximately 500,000 years. It sits in an area of the disc

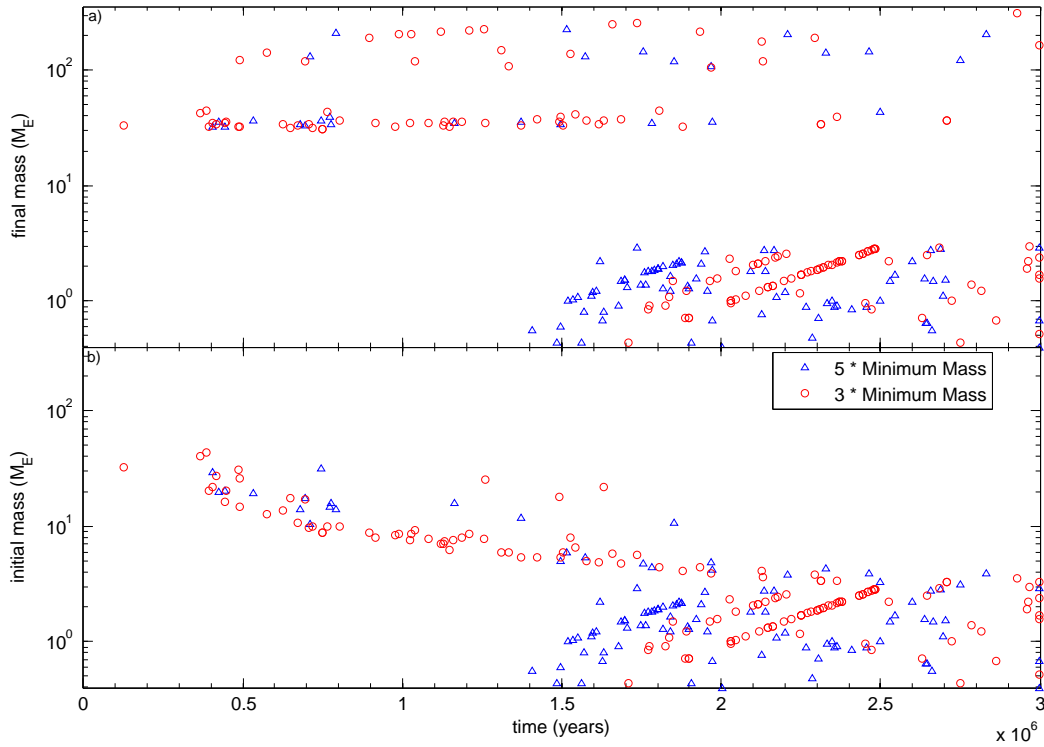


Figure 15. Summary of final masses and initial masses against time of loss for all planets that were lost beyond 0.1 AU.

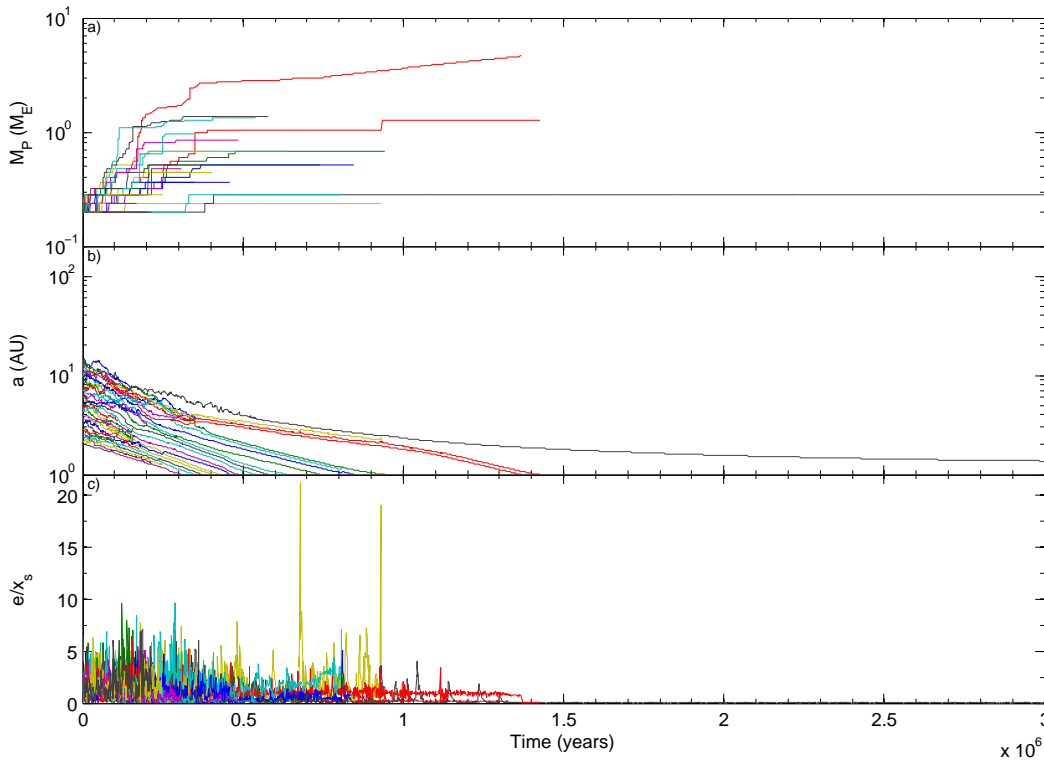
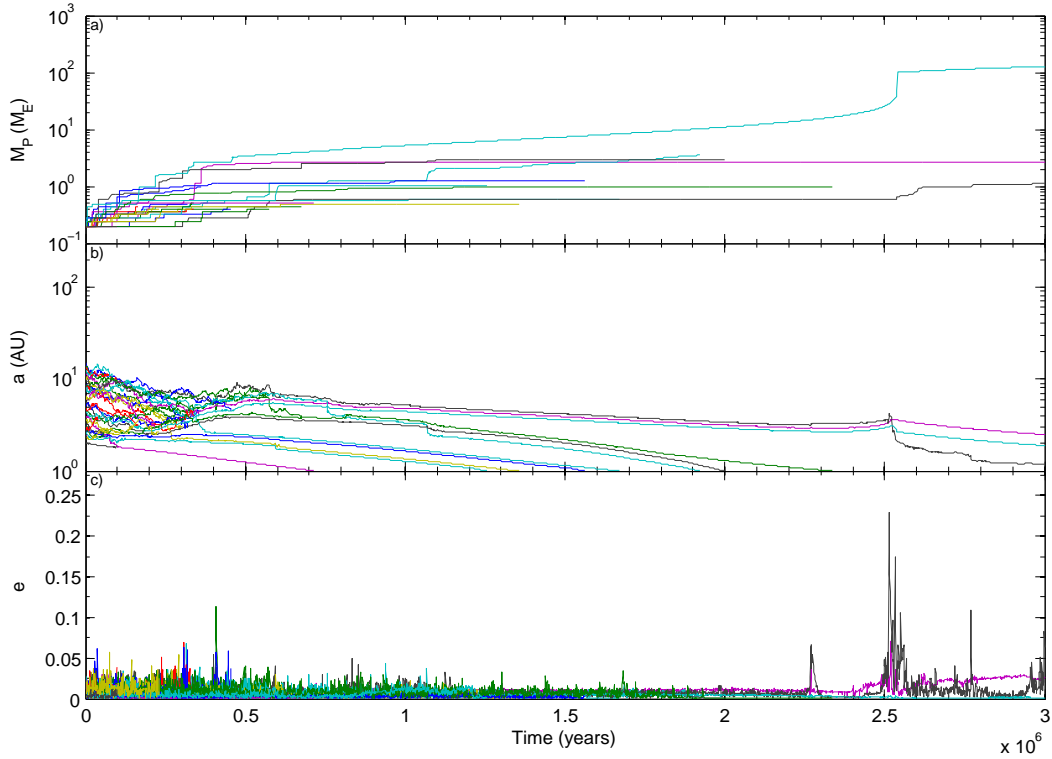
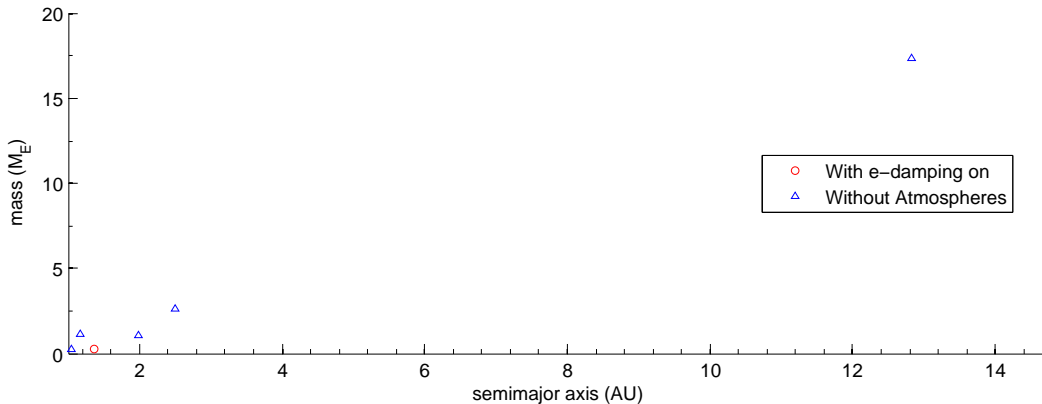


Figure 16. Evolution of masses, semimajor axes and eccentricities of all protoplanets in simulation E02B.



**Figure 17.** Evolution of masses, semimajor axes and eccentricities of all protoplanets in simulation M03B-NA.



**Figure 18.** Summary of masses against semimajor axis for all small surviving planets outside 1 AU for both runs where eccentricity damping was turned off and where enhanced capture radii due to atmospheric drag were turned off.

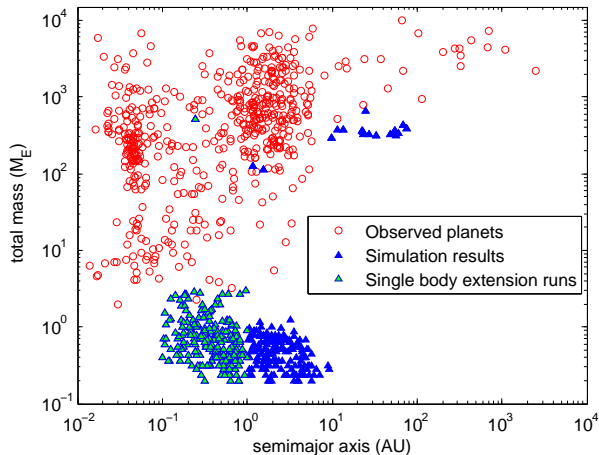
largely cleared of solid material by other protoplanets and slowly accretes gas before eventually undergoing runaway gas accretion at 2.5 Myrs and ends up at 2 AU with a mass of  $126 M_{\oplus}$ .

Run M07B-NA forms a gas giant by means of three  $1\text{--}1.5 M_{\oplus}$  bodies migrating out to large semimajor axes, and then merging to form a  $3.5 M_{\oplus}$  body at 40 AU which slowly accretes gas until runaway gas accretion occurs at 2.8 Myrs. The planet ends up at 50 AU with a mass of  $319 M_{\oplus}$ . The lower mass planets that survived in these runs are shown in Fig. 18. Interestingly, one of these is a Neptune-sized planet.

## 5 COMPARISON WITH OBSERVATIONS

The work presented in this paper is not intended to be a serious attempt at planetary population synthesis modelling, unlike the work presented by Ida & Lin (2008) and Mordasini et al. (2009b). Instead it is aimed at exploring the consequences of having strong corotation torques operating during the oligarchic growth stage of planetary systems formation, and understanding how planetary growth, migration and planet-planet interactions combine to form planetary systems. Nonetheless, it is of interest to examine how well the simple models that we have presented compare with the observational data on extrasolar planets.

Figure 19 shows a mass-period diagram with our re-

**Figure 19.** Mass vs semimajor axis plot comparing observed extrasolar planets with our simulation results.

sults overlaid on all current observed exoplanets (sourced from [www.exoplanet.eu](http://www.exoplanet.eu)). Our shorter period giant planets lie well in the range of already detected exoplanets both in terms of mass and semimajor axis. Our longer period planets, however, lie in an area that is sparsely populated with observational results. It is worth noting, however, that this region of parameter space is much more problematic for the detection of planets, as observations rely on direct imaging methods rather than radial velocity or transit observations.

A clear failing of our results is in the formation of super-Earths and Neptune-mass bodies. One reason for this appears to be the gas accretion routine that we have adopted, that allows planets to accrete gas once their masses exceed  $3 M_{\oplus}$ . An additional issue is the adoption of atmosphere-induced enhanced capture radii for planetesimal accretion onto protoplanets. The very rapid growth of planets due to this often causes them to migrate rapidly toward the central star, an outcome that is reduced in models where enhanced capture radii are not included. These are issues that we will address in a future publication.

## 6 DISCUSSION AND CONCLUSIONS

Although the models presented in this paper include a broad range of physical processes relevant to planet formation (migration; planetary growth through mutual protoplanet collisions; accretion of planetesimals and gas; planet-planet gravitational interactions), we have adopted a number of assumptions and simplifications that inevitably affect the realism of the simulations and their results. These include:

(i) *Simulation domain.* Even though we have modelled a relatively wide semimajor axis domain with our initial solid matter disc compared to previous N-body work on planetary formation, it is clear that accurate modelling of discs in which significant corotation torques arise requires as wide a domain as possible. Protoplanets move significantly in the disc with some forming at 2-3 AU and migrating out to 70-80 AU. Similarly, planets migrate inward and ought to traverse the terrestrial planet region which we have not modelled. Planets forming in the terrestrial region might also migrate out into the regions that we have investigated. In short, the

migration behaviour observed in the simulations presented in this paper indicates that all regions of the disc are coupled during planet formation, and it is no longer sensible to think in terms of a “terrestrial planet region” or a “giant planet region”. As such, a suitable model would involve a domain ranging from as far in as 0.1 AU out to approximately 50 AU. Such a simulation is beyond current modelling techniques because of the required numbers of protoplanets and planetesimals, even for the method presented by McNeil & Nelson (2009, 2010) which utilises multiple time steps in a parallel symplectic integrator. Instead, such global models of planetary formation are probably going to require efficient use of modern GPU technology.

(ii) *Gas disc model.* We currently model the gas disc as having fixed power-laws in surface density and temperature, with the disc mass undergoing exponential decay to mimic its viscous and photoevaporative evolution. In reality, the disc is heated by the central star and through local viscous dissipation, and it cools through radiative emission. A significant improvement to the model that we are in the process of implementing will be to evolve the disc surface density and temperature explicitly using a 1+1D numerical solution, as described in Papaloizou & Terquem (1999), for example. This approach will be similar to that described in Fogg & Nelson (2009) and references therein, and will allow gap formation and type II migration to be simulated directly, along with UV photoevaporation of the disc during its final stages of dispersal.

(iii) *Planetary atmosphere model and enhanced capture radii.* As described in the preceding sections, rapid planetary growth is assisted by the enhanced accretion of planetesimals through implementation of a model for planetary atmospheres that increases the effective accretion cross section (Inaba & Ikoma 2003). Although this model works well when accretion is dominated by planetesimals, it is probably inaccurate when accretion includes giant impacts between protoplanets. In particular, a planetary atmosphere can be completely liberated from a planet when it is impacted by a body whose mass is similar to that of the atmosphere, and our implementation of the atmosphere model does not account for this effect. The atmosphere model would clearly be improved in its accuracy if it responded to giant impacts as well as planetesimal accretion rates.

(iv) *Gas envelope accretion.* Our model for gas accretion during the formation of gas giants is very rudimentary, although it serves the purpose of allowing gas giant planets to form in our simulations. While a full accretion model for each planet similar to those presented in Pollack et al. (1996) and Movshovitz et al. (2011) would be ideal, this is computationally beyond the reaches of an N-body code that can model planetary systems formation over Myr time scales. However, there are improvements that can be made that will allow local conditions in the disc to influence the gas accretion rate onto a planet. Coupled with a more sophisticated disc model that allows explicit modelling of gap formation and gas accretion, such an approach would alleviate the requirement to set an artificial upper limit for the planet mass that can form through runaway gas accretion.

We have presented the results of simulations that include recent torque formulae for type I migration (including Lindblad and corotation torques), with gas envelope accre-

tion, enhanced capture radii due to gas atmospheres, and planet-planet gravitational dynamics included. We have surveyed a range of disc models which all allow for outward migration driven by corotation torques. The main results that we have obtained may be summarised as follows:

- Convergent migration of protoplanets, and the rapid accretion of planetesimals, can cause the rapid growth of planetary cores to masses in excess of  $10 M_{\oplus}$  within 0.5 Myr in most disc models. This leads to rapid inward migration of these bodies, driven by Lindblad torques, when the horseshoe libration time scale becomes significantly shorter than the thermal/viscous diffusion time scale and the corotation torques saturate.

- Formation of planetary cores with a few Earth masses  $\geq 0.5$  Myr after the simulations are initiated can lead to their migration into the outer regions of the disc (30 - 50 AU). Steady mass growth through gas accretion onto the planet can counterbalance the slow inward migration that occurs as the gas disc mass reduces, and long-term survival in the outer disc can lead to gas giant planet formation there when runaway gas accretion ensues. This mode of giant planet formation was found to be a common outcome in our simulations, especially those with disc models that generate strong outward migration, leading to numerous gas giant planets being formed between semimajor axes 10 - 60 AU. Models such as these could potentially explain the long-period giant planets discovered recently through direct imaging (Marois et al. 2010; Kalas et al. 2008; Lagrange et al. 2010).

- Out of 40 simulations that used disc models whose masses were either 3 or 5 times more massive than the MMSN, 19 gas giant planets were formed. Most of these are similar in mass to Jupiter (in part because of the gas accretion prescription that was adopted in the models), and are formed at large distances from the star. Short period Jovian mass planets were also formed, however, along with a pair of Saturn-mass bodies at intermediate ( $\sim 1$  AU) orbit distances. These latter systems were formed in discs that generate weaker corotation torques than those that tend to generate the longer-period giant planets.

- Multiplanet systems containing more than one giant planet were found to be a rare outcome (3 out of 40 simulations produced two giant planets each), and this has the additional effect of producing systems with very small eccentricities and inclinations due to the low rate of occurrence of planet-planet scattering events. In fact, the only planets to be formed with significant eccentricities were a pair of closely separated Jovian-mass objects that underwent significant dynamical interaction.

- Our simulations completely fail to produce super-Earth or Neptune-mass planets. This appears to arise because of very rapid inward migration of planets that grow early in the disc lifetime and undergo rapid inward migration, combined with the switching-on of gas accretion that converts planets of intermediate mass into gas giants at later times. Modification of the planetary atmosphere and gas accretion prescriptions will probably result in more surviving planets with intermediate masses. Numerous planets in the Earth mass range were formed in the simulations, however. The ‘desert’ of super-Earths and Neptunes is similar to that reported in the planetary population synthesis models of Ida & Lin

(2008), and occurs for much the same reasons as theirs (rapid gas accretion and migration).

- Simulations performed where the corotation torque is attenuated when planet eccentricities grow to become larger than the dimensionless horseshoe width appear to produce results quite different from those in which this effect is neglected (i.e. all the runs described above). In particular the growth and survival of planets is reduced because mutual encounters between protoplanets maintains the typical eccentricities above the critical value for which corotation torques diminish. In these latter simulations, no gas giant planets were formed at all. Further work is required to establish the influence of corotation torques on planet formation *via* oligarchic growth, where planet-planet interactions maintain finite values of the eccentricity.

Our models demonstrate that strong corotation torques can substantially alter the qualitative outcomes of planet formation simulations. Even the simplest model of planet formation that involves non linear gravitational interaction between protoplanets and planetesimals during planetary accumulation is by its nature a chaotic process. Given a well-defined distribution of initial protoplanet/planetesimal masses and orbital elements from which individual formation models are drawn, however, an ensemble of such models should give rise to a distribution of outcomes with well-defined statistical properties. Allowing the set of initial conditions to be drawn from a range of disc models whose lifetimes and radial profiles of density and temperature also have well-defined distributions serves only to modify the distribution of outcomes, as does including additional physical processes such as type I migration. A corollary of this argument is that increasing the complexity of migration processes, as we have done in this paper, also serves to modify the distribution of outcomes in a quantifiable manner. Corotation torques, however, increase the dependency of formation outcomes on the details of the underlying disc model and microphysical processes such as those that control the opacity of disc material. The dependency of migration on opacity, turbulent viscosity and other disc properties, and the role of migration in shaping planetary system architectures, increases the need for more refined observations of protoplanetary disc properties and improved disc models to allow planetary formation calculations to be compared with data on extrasolar planetary systems in a meaningful way. To summarise: planetary formation is a chaotic process, but is deterministic in a statistical sense. Corotation torques do not change the validity of this statement, however, their dependence on detailed disc properties increases the difficulty of constructing realistic planetary formation models for comparison with observational data.

This is the first in a series of papers to examine the oligarchic growth of planets under the influence of type I migration, including corotation torques. Models that include a more sophisticated treatment of the issues raised in Sect. 6 will be presented in a forthcoming publication.

## ACKNOWLEDGMENTS

P. Hellary is supported by a QMUL PhD studentship. The simulations presented in this paper were performed on the High Performance Computing facility at QMUL purchased

under the SRIF and CIF initiatives. We acknowledge useful discussions with D. McNeil concerning various aspects of this paper.

## REFERENCES

- Adachi, I., Hayashi, C., & Nakazawa, K. 1976, *Prog. Theor. Phys.*, 56, 1756
- Batalha N. M., Borucki W. J., Bryson T. B., Buchhave L. A., Caldwell D. A., Christensen-Dalsgaard J., Ciardi D., Dunham E. W. et al., 2011, *ApJ*, 729, 27
- Bell K. R., Cassen P. M., Klahr H. H., Henning T., 1997, *ApJ*, 486, 372
- Bell K. R., Lin D. N. C., 1994, *ApJ*, 427, 987
- Bitsch B., Kley W., 2010, *A&A*, 523, A30
- Bonfils X., Forveille T., Delfosse X., Udry S., Mayor M., Perrier C., Bouchy F., Pepe F. et al., 2005, *A&A*, 443, L15
- Bryden G., Chen X., Lin D. N. C., Nelson R. P., Papaloizou J. C. B., 1999, *ApJ*, 514, 344
- Butler R. P., Vogt S. S., Marcy G. W., Fischer D. A., Wright J. T., Henry G. W., Laughlin G., Lissauer J. J., 2004, *ApJ*, 617, 580
- Chambers, J. E. 1999, *MNRAS*, 304, 793
- Clarke C. J., Gendrin A., Sotomayor M., 2001, *MNRAS*, 328, 485
- Cresswell P., Nelson R. P., 2006, *A&A*, 450, 833
- Daisaka, J. K., Tanaka, H., Ida, S. 2006, *Icarus*, 185, 492
- D'Angelo, G., Kley, W., & Henning, T. 2003, *ApJ*, 586, 540
- Fischer D. A., Marcy G. W., Butler R. P., Vogt S. S., Laughlin G., Henry G. W., Abouav D., Peek K. M. G. et al., 2008, *ApJ*, 675, 790
- Fogg M. J., Nelson R. P., 2009, *A&A*, 498, 575
- Fogg M. J., Nelson R. P., 2007, *A&A*, 472, 1003
- Goldreich, P., & Tremaine, S. 1979, *ApJ*, 233, 857
- Hayashi, C. 1981, *Prog. Theor. Phys. Suppl.*, 70, 35
- Ida S., Lin D. N. C., 2010, *ApJ*, 719, 810
- Ida S., Lin D. N. C., 2008, *ApJ*, 673, 487
- Inaba, S., & Ikoma, M. 2003, *A&A*, 410, 711
- Ivanov P. B., Papaloizou J. C. B., Polnarev A. G., 1999, *MNRAS*, 307, 79
- Kalas P., Graham J. R., Chiang E., Fitzgerald M. P., Clampin M., Kite E. S., Stapelfeldt K., Marois C. et al., 2008, *Sci*, 322, 1345
- Kley W., 1999, *MNRAS*, 303, 696
- Lagrange A.-M., Bonnefoy M., Chauvin G., Apai D., Ehrenreich D., Boccaletti A., Gratadour D., Rouan D. et al., 2010, *Sci*, 329, 57
- Léger A., Rouan D., Scheider J., Barge P., Fridlund M., Samuel B., Ollivier M., Guenther E. et al., 2009, *A&A*, 506, 287
- Lin D. N. C., Papaloizou J., 1986, *ApJ*, 307, 395
- Lissauer J. J., 1993, *ARA&A*, 31, 129
- Lissauer J. J., Fabrycky D. C., Ford E. B., Borucki W. J., Fressin F., Marcy G. W., Orosz J. A., Rowe J. F. et al., 2011, *Nat*, 470, 53
- Lyra W., Paardekooper S.-J., Mac Low M.-M., 2010, *ApJ*, 715, L68
- Marois C., Zuckerman B., Konopacky Q. M., Macintosh B., Barman T., 2010, *Nat*, 468, 1080
- Masset F. S., 2002, *A&A*, 387, 605
- Masset F. S., 2001, *ApJ*, 558, 453
- Mayor M., Queloz D., 1995, *Nat*, 378, 355
- McNeil D. S., Nelson R. P., 2010, *MNRAS*, 401, 1691
- McNeil D. S., Nelson R. P., 2009, *MNRAS*, 392, 537
- McNeil D., Duncan M., Levison H. F., 2005, *AJ*, 130, 2884
- Miguel Y., Guilera O. M., Brunini A., 2011, *MNRAS*, 412, 2113
- Mordasini C., Alibert Y., Benz W., 2009a, *A&A*, 501, 1139
- Mordasini C., Alibert Y., Benz W., Naef D., 2009b, *A&A*, 501, 1161
- Movshovitz, N., Bodenheimer, P., Podolak, M., Lissauer, J. J. 2011, *Icarus*, 209, 616
- Nelson R. P., Papaloizou J. C. B., Masset F., Kley W., 2000, *MNRAS*, 318, 18
- Paardekooper S.-J., Baruteau C., Crida A., Kley W., 2010, *MNRAS*, 401, 1950
- Paardekooper S.-J., Baruteau C., Kley W., 2011, *MNRAS*, 410, 293
- Paardekooper S.-J., Papaloizou J. C. B., 2008, *A&A*, 485, 877
- Papaloizou J. C. B., Larwood J. D., 2000, *MNRAS*, 315, 823
- Papaloizou, J. C. B., & Terquem, C. 1999, *ApJ*, 521, 823
- Pollack, J. B., Hubickyj, O., Bodenheimer, P., Lissauer, J. J., Podolak, M., & Greenzweig, Y. 1996, *Icarus*, 124, 62
- Sicilia-Aguilar, A., Hartmann, L. W., Briceño, C., Muzerolle, J., & Calvet, N. 2004, *AJ*, 128, 805
- Syer D., Clarke C. J., 1995, *MNRAS*, 277, 758
- Terquem C., Papaloizou J. C. B., 2007, *ApJ*, 654, 1110
- Thommes, E. W., Duncan, M. J., & Levison, H. F. 2003, *Icarus*, 161, 431
- Ward W. R., 1991, *Abstr. Lunar Planet. Sci. Conf.*, 22, 1463
- Ward, W. R. 1997, *Icarus*, 126, 261